

THE LONG-TERM X-RAY VARIABILITY OF BROAD ABSORPTION LINE QUASARS

C. SAEZ^{1,2,3}, W. N. BRANDT^{1,2}, S. C. GALLAGHER⁴, F. E. BAUER^{3,5}, AND G. P. GARMIRE¹

Draft version November 5, 2018

ABSTRACT

We analyze the long-term (rest-frame 3–30 yr) X-ray variability of eleven broad absorption line (BAL) quasars, mainly to constrain the variation properties of the X-ray absorbing shielding gas that is thought to play a critical role in BAL wind launching. Our BAL quasar sample has coverage with multiple X-ray observatories including *Chandra*, *XMM-Newton*, *BeppoSAX*, *ASCA*, *ROSAT*, and *Einstein*; 3–11 observations are available for each source. For seven of the eleven sources we have obtained and analyzed new *Chandra* observations suitable for searching for any strong X-ray variability. We find highly significant X-ray variability in three sources (PG 1001+054, PG 1004+130, and PG 2112+059). The maximum observed amplitude of the 2–8 keV variability is a factor of 3.8 ± 1.3 , 1.5 ± 0.2 , and 9.9 ± 2.3 for PG 1001+054, PG 1004+130, and PG 2112+059, respectively, and these sources show detectable variability on rest-frame timescales down to 5.8, 1.4, and 0.5 yr. For PG 1004+130 and PG 2112+059 we also find significant X-ray spectral variability associated with the flux variability. Considering our sample as a whole, we do not find that BAL quasars exhibit exceptional long-term X-ray variability when compared to the quasar population in general. We do not find evidence for common strong changes in the shielding gas owing to physical rearrangement or accretion-disk rotation, although some changes are found; this has implications for modeling observed ultraviolet BAL variability. Finally, we report for the first time an X-ray detection of the highly polarized and well-studied BAL quasar IRAS 14026+4341 in its new *Chandra* observation.

Subject headings: cosmology: observations — X-rays: galaxies — galaxies: active — quasars: absorption lines

1. INTRODUCTION

Fast outflows are common in active galactic nuclei (AGNs) over a range of more than 10,000 in AGN luminosity (e.g., Laor & Brandt 2002; Ganguly & Brotherton 2008). These outflows are a significant component of the nuclear environment, and their ubiquity suggests that mass ejection in a wind is fundamentally linked to mass accretion onto a supermassive black hole (SMBH). Indeed, outflows may be key in allowing the accreting matter to expel angular momentum. Observationally, while these outflows are most commonly studied via the absorption features they imprint upon ultraviolet (UV) and X-ray spectra, they are also thought to shape emission-line and continuum properties (e.g., Murray & Chiang 1997; Richards et al. 2011). Studies of the outflows from luminous AGNs, such as those seen in Broad Absorption Line (BAL) quasars, have taken on further importance in recent years as they are one of the possible agents of feedback in typical massive galaxies (e.g., Di Matteo et al. 2005). Outflows from luminous AGNs may expel enough gas from the SMBH/galaxy system to quench both SMBH growth and star formation, perhaps leading to the observed relations between SMBH and bulge properties (e.g., Gültekin et al. 2009).

One frequently used and generally well-supported

model proposes that the UV absorption lines of BAL quasars originate in a line-driven wind that is launched from the accretion disk at $\approx 10^{16-17}$ cm from the SMBH (e.g., Murray et al. 1995; Proga et al. 2000). In this model, the weak X-ray emission seen from BAL quasars (e.g., Gallagher et al. 2006; Gibson et al. 2009) is due to absorption in stalled, highly ionized “shielding gas” at smaller radii that protects the wind from nuclear extreme UV and soft X-ray radiation; without such an absorbing layer, these energetic photons would so highly ionize the potential wind material that it could not be effectively accelerated via line pressure. Supporting observational evidence for the physical importance of the shielding gas comes in the form of correlations between the X-ray weakness of BAL quasars and the strength and velocity of their UV C IV BALs (e.g., Gallagher et al. 2006; Gibson et al. 2009; Wu et al. 2010).

The nature of the shielding gas in BAL quasars remains poorly constrained observationally. Heavy X-ray absorption is directly seen in many of the BAL quasars with X-ray spectra of reasonable quality (e.g., Gallagher et al. 2001, 2002; Fan et al. 2009). Measured absorption column densities span a broad range of typically $N_{\text{H}} \approx 10^{22-24}$ cm⁻², although most individual N_{H} measurements have significant uncertainties owing to limited photon statistics and absorption complexity (e.g., ionization and partial-covering effects). The kinematics of the X-ray absorber in BAL quasars is also poorly constrained. The X-ray absorber is sometimes envisioned to be a stalled “sacrificial wind” that protects the UV-absorbing wind launched at larger radii (e.g., Proga et al. 2000), although in one BAL quasar apparent evidence for a rapidly outflowing X-ray absorber has been found (e.g., Chartas et al. 2009; Saez & Chartas 2011). Mag-

¹ Department of Astronomy & Astrophysics, The Pennsylvania State University, University Park, PA 16802, USA

² Institute for Gravitation and the Cosmos, The Pennsylvania State University, University Park, PA 16802, USA

³ Pontificia Universidad Católica de Chile, Departamento de Astronomía y Astrofísica, Casilla 306, Santiago 22, Chile

⁴ Department of Physics and Astronomy, The University of Western Ontario, London, ON N6A 3K7, Canada

⁵ Space Science Institute, 4750 Walnut Street, Suite 205, Boulder, CO 80301, USA

netocentrifugal effects, as well as radiative ones, may play an important role in setting the kinematics of the X-ray absorbing shielding gas (e.g., Everett 2005).

Remarkable X-ray absorption variability has been seen in a few BAL quasars (e.g., Gallagher et al. 2004; Schartel et al. 2005, 2007; Miller et al. 2006; Chartas et al. 2009), typically on multi-year timescales, indicating that the X-ray absorber is indeed a dynamical structure. This variability could be due simply to accretion-disk rotation moving an azimuthally asymmetric X-ray absorber through our line of sight; at the expected radius of the shielding gas ($\lesssim 10^{15-16}$ cm), substantial fractional disk rotation is expected on multi-year timescales. The results on X-ray absorption variability in BAL quasars are broadly reminiscent of those found for lower luminosity Seyfert 2 galaxies, where X-ray absorbing column densities are found to vary commonly (e.g., Risaliti et al. 2002, 2009). In addition to variations in X-ray absorber column density, some BAL quasars with multiple observations have also shown notable continuum luminosity variability. For example, the normalization of the power-law continuum in PG 2112+059 decreased by a factor ≈ 3.5 between 1999 and 2002 (Gallagher et al. 2004), and continuum variability of this magnitude continued through 2007 (Schartel et al. 2010).

Current studies of the X-ray absorption variability of BAL quasars suffer from small sample sizes. Presently only a handful of BAL quasars have sensitive coverage in multiple X-ray observations, and thus the general frequency of BAL quasar X-ray variability remains poorly characterized. In order to improve this situation, we targeted seven optically bright BAL quasars as part of *Chandra* Cycle 11 that already had sensitive archival X-ray observations with *Chandra*, *XMM-Newton*, or earlier missions. We obtained relatively short observations (5–7 ks) suitable for searching for any strong X-ray variability. Our main goal was to execute an economical multi-year X-ray variability search for as many objects as possible, so that the basic X-ray variability properties of BAL quasars could be characterized as a class. Similar ongoing efforts are also now characterizing the multi-year UV absorption-line variability of BAL quasars (e.g., Gibson et al. 2008, 2010; Capellupo et al. 2011, 2012; Filiz Ak et al. 2012), and X-ray constraints upon shielding gas variations will inform these efforts. In addition to presenting our new *Chandra* Cycle 11 observations below, we also utilize the existing archival X-ray observations of BAL quasars capable of constraining long-term X-ray variability; this maximizes our sample size.

The layout of this paper is as follows: in §2 we describe the sample and the X-ray data reduction; in §3 we provide a description of the spectral analysis; in §4 we provide our variability results and discussion focusing on long-term X-ray variability; and in §5 we summarize our main findings. Throughout this paper, unless stated otherwise, we use cgs units, the errors listed are at the 1σ level, and we adopt a flat Λ -dominated universe with $H_0 = 70$ km s $^{-1}$ Mpc $^{-1}$, $\Omega_\Lambda = 0.7$, and $\Omega_M = 0.3$.

2. OBSERVATIONS AND DATA REDUCTION

Our sample consists of eleven BAL quasars that have been observed in the past by sensitive X-ray missions including *Chandra*, *XMM-Newton*, *BeppoSAX*, *ASCA*, *ROSAT*, and *Einstein*. Seven of these BAL quasars

have been re-observed with new short-exposure (5–7 ks) *Chandra* observations that are analyzed in this paper. In Table 1 we present the Galactic column densities, radio-loudness parameters (R_L),⁶ and some basic optical and radio properties for our sample. The redshifts of our sample quasars range from 0.04–2.88. The only sources that are not radio-quiet quasars (RQQs; $R_L \leq 10$) are PG 1004+130 and Mrk 231, radio-loud quasars (RLQs) with $R_L > 10$. Notice, however, that in the case of Mrk 231 there is likely substantial reddening ($A_V \sim 2$; e.g., Boksenberg et al. 1977); as a consequence the intrinsic 4400 Å flux density would be approximately an order of magnitude higher. Based on this argument Mrk 231 would not be considered a bona-fide RLQ.

In Table 1 we also present the number of X-ray observations of each source and the rest-frame time span coverage. The distributions of the number of X-ray observations with the respective rest-frame time span coverage are presented in Figure 1. There are 3–11 X-ray observations with rest-frame time span ranging from 3–30 yr per source. The observation logs of the sources analyzed in this work, which include observation dates, observed count rates with 1σ error bars, and exposure times, are presented in Table 2 for the *Chandra*, *BeppoSAX*, *ROSAT*, and *Einstein* observations; Table 3 for the *XMM-Newton* observations; and Table 4 for the *ASCA* observations. The errors on the source counts were computed by propagating the asymmetric errors on the total and background counts using the approach described in §5 of Barlow (2004). The total and background count errors were obtained from Tables 1 and 2 of Gehrels (1986).

2.1. Chandra observations

The *Chandra* observations (new and archival) were analyzed using the standard software CIAO version 4.2 provided by the *Chandra* X-ray Center (CXC). Standard CXC threads were employed to screen the data for status, grade (*ASCA* grade 0, 2, 3, 4, and 6 events), and time intervals of acceptable aspect solution and background levels. For most of the observations the source and background spectra were extracted (using the CIAO task DMEXTRACT) from a circular region with an aperture radius of 4''⁷ and an annular source-free region with an inner radius of 6'' and an outer radius of 24'', respectively. For the cases of PG 1004+130 and Mrk 231 the source, annulus inner, and annulus outer radii are (16'', 20'', 30'') and (24'', 30'', 50''), respectively. For these sources we have selected larger extraction regions given that they possess extended X-ray emission. The extended emission of PG 1004+130 and Mrk 231 has been studied by Miller et al. (2006) and Gallagher et al. (2002), respectively. We selected the radius of extraction for these sources using a fixed background region (annular region of inner radius 40'' and outer radius 60'') and estimating the total counts as a function of aperture radius. The aperture radius selected corresponds to that where the total counts reach an approximately constant

⁶ The radio-loudness parameter is defined as the ratio between the flux density at 5 GHz and the flux density at 4400 Å in the rest frame of the source (Kellermann et al. 1989).

⁷ The 1.5 keV encircled energy at 4'' from the center of an on-axis point source is $\sim 99\%$ for ACIS-S.

TABLE 1
OPTICAL/RADIO PROPERTIES, GALACTIC COLUMN DENSITIES, AND X-RAY COVERAGE OF SURVEYED BAL QUASARS

OBJECT NAME	z	$\alpha_{2000.0}^a$	$\delta_{2000.0}^a$	N_{HGal}^b	AB ₂₅₀₀ ^c	$\log R_L^d$	BAL type ^e	$N_{\text{X-ray}}^f$	Δt_{rest}^f
IRAS 07598+6508	0.148	08 04 30.51	+64 59 52.7	4.3	14.5	0.80	Lo	5	16.8
PG 0946+301	1.221	09 49 41.10	+29 55 19.2	1.7	16.2	-1.71	Hi	3	7.3
PG 1001+054	0.160	10 04 20.14	+05 13 00.5	2.4	16.6	-0.12	Hi	5	26.0
PG 1004+130	0.241	10 07 26.11	+12 48 56.1	3.7	15.3	2.18	Hi	3	19.9
Q 1246-057	2.247	12 49 13.86	-05 59 19.1	2.1	16.3	<-0.14	Hi	8	7.7
Mrk 231	0.042	12 56 14.23	+56 52 25.2	1.3	15.3	1.41	Lo	11	28.4
IRAS 14026+4341	0.323	14 04 38.80	+43 27 07.4	1.2	16.2	-0.27	Lo	4	13.6
CSO 755	2.882	15 25 53.89	+51 36 49.2	1.6	16.2	<-0.19	Hi	5	2.9
SBS 1542+541	2.370	15 43 59.45	+53 59 03.4	1.3	16.8	-0.85	Hi	4	2.5
PG 1700+518	0.292	17 01 24.80	+51 49 20.0	2.6	15.3	0.38	Lo	6	15.0
PG 2112+059	0.466	21 14 52.57	+06 07 42.5	6.6	15.0	-0.56	Hi	9	10.9

^a Optical positions in J2000.0 equatorial coordinates.

^b Galactic absorption column densities in units of 10^{20} cm^{-2} (from Dickey & Lockman 1990), obtained using the optical coordinates of the sources and the HEASARC N_{H} tool at <http://heasarc.gsfc.nasa.gov/cgi-bin/Tools/w3nh/w3nh.pl>

^c The monochromatic AB magnitude at rest-frame wavelength 2500 Å. These were computed from the flux densities obtained from the closest optical magnitude found in the NASA Extragalactic Database (NED; <http://ned.ipac.caltech.edu>) and extrapolating a power-law with $\alpha = -0.5$ (e.g., Vanden Berk et al. 2001). Previous to the extrapolation the flux densities obtained through NED have been corrected for Galactic reddening.

^d Logarithm of the radio-loudness parameter ($R_L = f_{5\text{GHz}}/f_{4400\text{Å}}$). The flux densities at rest-frame 4400 Å are obtained using the Galactic reddening corrected flux densities obtained from the closest optical magnitudes and extrapolating a power-law with $\alpha = -0.5$ (e.g., Vanden Berk et al. 2001). The flux densities at rest-frame 5 GHz have been obtained using either the flux densities at 1.4 GHz or the flux densities at 5 GHz. When both the 1.4 GHz and 5 GHz flux densities are available, we find the flux density at rest-frame 5 GHz through a power-law interpolation between the two values. For all the sources with the exception of SBS 1542+541 the flux densities at 1.4 GHz were obtained from the NVSS (Condon et al. 1998) or the FIRST survey (White et al. 1997). Additionally for PG sources the flux densities at 5 GHz were obtained from Kellermann et al. (1989). For SBS 1542+541 the flux densities at 1.4 GHz and 5 GHz were obtained from Petric et al. (2006).

^e Hi = ultraviolet spectra show high-ionization BALs only; Lo = low-ionization (Mg II and/or Al III) BALs present.

^f Number of X-ray observations ($N_{\text{X-ray}}$) with their rest-frame time span coverage in years (Δt_{rest}).

value. The use of larger source regions for the *Chandra* observations of PG 1004+130 and Mrk 231 is necessary in order to make fair flux comparisons with the other X-ray missions that have more limited angular resolution. The numbers of counts in the source regions at energies of 0.5–8 keV are presented in Table 2. The response files used to analyze the source spectra were created with the CIAO tasks MKACISRMF for the redistribution matrix files (RMFs) and MKARF for the ancillary response files (ARFs).

2.2. XMM-Newton observations

The *XMM-Newton* data were analyzed with the Science Analysis Software (SAS) version 10.0.0 provided by the *XMM-Newton* Science Operations Centre (SOC). The events files were obtained by including the events with flag = 0, pattern ≤ 12 (pattern ≤ 4), and $200 \leq \text{PI} \leq 12,000$ ($150 \leq \text{PI} \leq 15,000$) for the MOS (pn) detectors. The events files were also temporally filtered in order to remove periods of flaring activity. To filter the events files for periods of flaring activity, we created light curves using single events with energies greater than 10 keV. Using these light curves we find and remove from the events files the time periods where the count rate is above 0.5 count s^{-1} for the MOS cameras and 1 count s^{-1} for the pn camera. For the three EPIC detectors (MOS1, MOS2, and pn), the source counts for each quasar were extracted from a circular region with an aperture radius of either $18''$ or $30''$.⁸ The default aperture radius of the source extraction region was $30''$;

⁸ The 1.5 keV encircled energy at $18''$ ($30''$) from the center of an on-axis point source is $\approx 75\%$ ($\approx 85\%$) for the EPIC cameras. The aperture corrections for the EPIC cameras are performed through the use of the ARFGEN routine.

however, when the background counts were $> 20\%$ of the total counts inside this region an aperture radius of $18''$ was used. Under this criterion most observations were reduced using $18''$ apertures. The cases that were reduced with $30''$ apertures were the 2001 December 8th observation of CSO 755, the Mrk 231 observation, the PG 1001+054 observation, and the 2003 May 14 observation of PG 2112+059. The background spectra for most of the sources were extracted from annular source-free regions with $50''$ inner radii and $100''$ outer radii. In cases where this region covered other X-ray sources or detector gaps, the background was extracted from a source-free circular region with radius $80''$ in the vicinity of the source. The numbers of counts in the source regions for the *XMM-Newton* cameras are presented in Table 3. These counts are selected at energies of 0.5–10 keV for the MOS cameras and 0.3–10 keV for the pn camera. The response files used to analyze the source spectra were created with the SAS tasks RMFGEN for the RMFs and ARFGEN for the ARFs.

2.3. ROSAT observations

The *ROSAT* PSPC observations were analyzed following the *ROSAT* XSELECT guide.⁹ Using the prescription given we applied all the standard corrections (gain variations, gain saturation, analog-to-digital nonlinearity, and dead time) to obtain cleaned events which were used for the subtraction of the source and background spectra. The source spectra were extracted from circular regions with aperture radii of $50''$. The background spectra for most of the sources were extracted from annular source-free regions with $100''$ inner radii and $200''$ outer radii;

⁹ http://heasarc.nasa.gov/docs/rosat/ros_xselect_guide

TABLE 2
LOG OF *Chandra*, *BeppoSAX*, *ROSAT*, AND *Einstein* OBSERVATIONS

OBJECT NAME	OBS. DATE	EXP. TIME ^a (ks)	COUNTS ^{a,b}	RATE (10^{-3} s^{-1})	Ref. ^c
New <i>Chandra</i> observations (0.5–8 keV)					
IRAS 07598+6508	2010 Jun 18	6.7	32^{+7}_{-6}	$4.7^{+1.0}_{-0.8}$	1
PG 0946+301	2010 Jan 11	6.5	57^{+8}_{-8}	$8.8^{+1.3}_{-1.2}$	1
PG 1001+054	2010 Jan 11	4.9	13^{+5}_{-4}	$2.6^{+0.9}_{-0.7}$	1
Mrk 231	2010 Jul 11	4.8	247^{+19}_{-18}	$51.6^{+3.9}_{-3.7}$	1
IRAS 14026+4341	2010 Jul 28	6.7	6^{+4}_{-2}	$0.9^{+0.5}_{-0.3}$	1
CSO 755	2010 Mar 21	4.9	110^{+12}_{-10}	$22.4^{+2.3}_{-2.1}$	1
PG 1700+518	2010 Jun 26	6.7	14^{+5}_{-4}	$2.0^{+0.7}_{-0.5}$	1
Archival <i>Chandra</i> observations (0.5–8 keV)					
IRAS 07598+6508	2000 Mar 21	1.3	9^{+4}_{-3}	$6.7^{+3.1}_{-2.2}$	2
PG 1004+130	2005 Jan 5	41.1	1905^{+47}_{-46}	46.4 ± 1.1	3
Q 1246–057	2000 Feb 8	5.5	42^{+8}_{-6}	$7.6^{+1.4}_{-1.2}$	2
Mrk 231	2000 Oct 19	39.3	2059^{+53}_{-52}	52.5 ± 1.3	4
Mrk 231	2003 Feb 3	39.7	1947^{+48}_{-47}	49.1 ± 1.2	5
Mrk 231	2003 Feb 11	38.6	1900^{+48}_{-47}	49.2 ± 1.2	5
Mrk 231	2003 Feb 20	36.0	1754^{+47}_{-46}	48.7 ± 1.3	5
SBS 1542+541	2000 Mar 22	4.5	79^{+10}_{-9}	$17.3^{+2.2}_{-1.9}$	2
PG 2112+059	2002 Sep 1	56.9	836^{+30}_{-29}	14.7 ± 0.5	6
Archival <i>BeppoSAX</i> observations (1.8–10 keV)					
Mrk 231	2001 Dec 29	144.0	818 ± 36	5.7 ± 0.3	7
CSO 755	1999 Feb 02	35.2	53 ± 18	1.5 ± 0.5	8
Archival <i>ROSAT</i> observations (0.5–2 keV)					
IRAS 07598+6508	1991 Mar 17	7.9	18^{+7}_{-6}	2.2 ± 0.8	9
PG 0946+301	1993 Nov 14	11.8	< 7	< 0.6	1
PG 1001+054	1992 May 17	8.6	9^{+5}_{-4}	1.1 ± 0.5	10
Q 1246–057	1991 Dec 21	12.8	20 ± 8	1.6 ± 0.6	1
Q 1246–057	1992 Jul 17	2.8	< 4	< 1.5	11
Q 1246–057	1993 Jan 5	9.1	14^{+6}_{-5}	$1.6^{+0.6}_{-0.5}$	11
Q 1246–057	1993 Jun 22	43.6	59^{+13}_{-12}	1.4 ± 0.3	11
Mrk 231	1991 Jun 7	23.2	224^{+18}_{-17}	9.7 ± 0.8	12
IRAS 14026+4341	1992 Jul 18	6.2	< 5	< 0.8	1
SBS 1542+541	1993 Ago 14	5.5	25^{+7}_{-6}	$4.5^{+1.2}_{-1.0}$	11
PG 1700+518	1991 Feb 9	7.8	< 7	< 0.9	11
PG 2112+059	1991 Nov 30	11.7	52^{+9}_{-8}	$4.5^{+0.8}_{-0.7}$	13
Archival <i>Einstein</i> observations (0.16–3.5 keV)					
PG 1001+054	1979 Dec 02	1.6	< 15	< 9.4	14
PG 1004+130	1979 May 21	7.1	< 37	< 4.9	14, 15
Q 1246–057	1979 Jul 20	3.5	< 24	< 7.0	14
Mrk 231	1980 Dec 23	2.1	< 19	< 8.1	14

^a The counts correspond to the net photon counts (background subtracted). The exposure times and photon counts are obtained after screening the data.

^b For details about the aperture sizes used see §2. The errors on the source counts were computed by propagating the asymmetric errors on the total and background counts using the approach of Barlow (2004). The total and background count errors were obtained from Tables 1 and 2 of Gehrels (1986).

^c REFERENCES: (1) This work; (2) Green et al. (2001); (3) Miller et al. (2006); (4) Gallagher et al. (2002); (5) Gallagher et al. (2005); (6) Gallagher et al. (2004); (7) Braitto et al. (2004); (8) Brandt et al. (1999); (9) Lawrence et al. (1997); (10) Laor et al. (1997); (11) Green & Mathur (1996); (12) Rigopoulou et al. (1996); (13) Wang et al. (1996); (14) Wilkes et al. (1994); (15) Elvis & Fabbiano (1984).

TABLE 3
LOG OF *XMM-Newton* ARCHIVAL OBSERVATIONS

OBJECT NAME	OBS. DATE	EXPOSURE TIME ^a			MOS1 ^b		MOS2 ^b		pn ^b		REF. ^c
		MOS1	MOS2	pn	COUNTS	RATE $\times 10^3$	COUNTS	RATE $\times 10^3$	COUNTS	RATE $\times 10^3$	
		(ks)			(0.5–10 keV)		(0.5–10 keV)		(0.3–10 keV)		
IRAS 07598+6508	2001 Oct 24	18.6	18.5	14.2	84 ⁺¹² ₋₁₁	4.5 \pm 0.6	70 ⁺¹¹ ₋₁₀	3.8 ^{+0.6} _{-0.5}	268 ⁺²⁰ ₋₁₉	18.9 ^{+1.4} _{-1.3}	1
PG 1001+054	2003 May 04	11.3	11.3	8.8	78 ⁺¹¹ ₋₁₀	6.9 \pm 0.9	62 ⁺¹⁰ ₋₉	5.5 ^{+0.9} _{-0.8}	322 \pm 20	36.4 ^{+2.3} _{-2.2}	2
PG 1004+130	2003 May 04	21.5	21.5	18.5	567 ⁺²⁷ ₋₂₆	26.4 \pm 1.2	622 ⁺²⁸ ₋₂₇	28.9 ^{+1.3} _{-1.2}	1777 ⁺⁴⁷ ₋₄₆	98.3 ^{+2.6} _{-2.5}	3
Q 1246–057	2001 Jul 11	40.0	40.0	33.5	126 ⁺¹⁵ ₋₁₄	3.2 \pm 0.4	127 ⁺¹⁵ ₋₁₄	3.2 \pm 0.4	335 \pm 28	10.0 \pm 0.8	4
Q 1246–057	2004 Jul 15	46.4	47.0	34.8	141 \pm 16	3.0 ^{+0.4} _{-0.3}	123 ⁺¹⁶ ₋₁₅	2.6 \pm 0.3	351 \pm 25	10.1 \pm 0.7	5
Mrk 231	2001 Jun 07	21.4	21.4	17.2	774 ⁺³⁰ ₋₂₉	36.1 \pm 1.4	739 ⁺³⁰ ₋₂₉	34.5 \pm 1.4	2165 ⁺⁵¹ ₋₅₀	125.8 \pm 2.9	6
IRAS 14026+4341	2005 Nov 26	8.7	7.9	0.0	<10	<1.2	14 \pm 6	1.8 ^{+0.8} _{-0.7}	7
IRAS 14026+4341	2006 Jan 16	6.9	6.2	0.0	12 \pm 6	1.7 ^{+0.9} _{-0.8}	<8	<1.3	7
CSO 755	2001 Jul 30	2.2	2.2	0.0	29 ⁺⁷ ₋₆	13.1 ^{+3.1} _{-2.7}	41 ⁺⁸ ₋₇	18.7 ^{+3.5} _{-3.1}	8
CSO 755	2001 Dec 08	30.1	30.3	24.6	610 ⁺²⁸ ₋₂₇	20.3 \pm 0.9	578 ⁺²⁷ ₋₂₆	19.1 \pm 0.9	1820 ⁺⁴⁸ ₋₄₇	73.8 \pm 1.9	8
CSO 755	2001 Dec 13	4.5	3.7	2.0	74 \pm 10	16.3 ^{+2.3} _{-2.1}	57 ⁺⁹ ₋₈	15.2 ^{+2.4} _{-2.2}	120 ⁺¹⁴ ₋₁₃	61.0 ^{+7.0} _{-6.7}	8
SBS 1542+541	2002 Feb 03	8.4	8.5	2.4	99 ⁺¹² ₋₁₁	11.7 ^{+1.4} _{-1.3}	74 ⁺¹¹ ₋₁₀	8.7 ^{+1.3} _{-1.2}	98 ⁺¹² ₋₁₁	40.4 ^{+5.0} _{-4.6}	4
SBS 1542+541	2002 Feb 06	23.8	23.6	12.7	261 ⁺¹⁹ ₋₁₈	11.0 \pm 0.8	268 ⁺¹⁹ ₋₁₈	11.3 \pm 0.8	489 ⁺²⁵ ₋₂₄	38.5 \pm 1.9	4
PG 1700+518	2009 Dec 19	7.0	6.9	4.5	<7	<0.9	<8	<1.2	30 \pm 9	6.7 ^{+2.0} _{-1.9}	9
PG 1700+518	2009 Dec 31	14.1	12.8	7.9	<12	<0.9	14 \pm 7	1.1 ^{+0.6} _{-0.5}	53 ⁺¹² ₋₁₁	6.7 ^{+1.5} _{-1.4}	9
PG 1700+518	2010 Jan 02	19.3	18.8	15.4	32 ⁺⁹ ₋₈	1.7 ^{+0.5} _{-0.4}	20 \pm 8	1.1 \pm 0.4	87 \pm 14	5.6 \pm 0.9	9
PG 2112+059	2003 May 14	9.3	9.7	6.9	340 ⁺²¹ ₋₂₀	36.4 ^{+2.2} _{-2.1}	343 ⁺²¹ ₋₂₀	35.3 \pm 2.1	900 ⁺³⁴ ₋₃₃	130.0 ^{+4.9} _{-4.8}	10
PG 2112+059	2005 Nov 20	72.9	73.1	64.8	245 \pm 19	3.4 \pm 0.3	235 ⁺¹⁹ ₋₁₈	3.2 ^{+0.3} _{-0.2}	785 ⁺³⁴ ₋₃₃	12.1 \pm 0.5	10
PG 2112+059	2007 May 03	23.7	23.2	19.3	132 ⁺¹⁴ ₋₁₃	5.6 \pm 0.6	124 \pm 13	5.3 ^{+0.6} _{-0.5}	336 \pm 23	17.4 \pm 1.2	10
PG 2112+059	2007 May 19	59.3	74.2	43.9	293 ⁺²¹ ₋₂₀	4.9 ^{+0.4} _{-0.3}	372 ⁺²³ ₋₂₂	5.0 \pm 0.3	767 ⁺³⁴ ₋₃₃	17.5 \pm 0.8	10
PG 2112+059	2007 May 21	85.7	87.5	66.3	494 \pm 26	5.8 \pm 0.3	456 ⁺²⁵ ₋₂₄	5.2 \pm 0.3	1289 ⁺⁴² ₋₄₁	19.4 \pm 0.6	10
PG 2112+059	2007 Nov 05	50.2	49.0	43.0	190 \pm 17	3.8 \pm 0.3	200 \pm 17	4.1 ^{+0.4} _{-0.3}	590 ⁺³⁰ ₋₂₉	13.7 \pm 0.7	10

^a The exposure times and photon counts are obtained after screening the data for flaring.

^b For details about the source and background extraction regions see §2. The errors on the source counts were computed by propagating the asymmetric errors on the total and background counts using the approach of Barlow (2004). The total and background count errors were obtained from Tables 1 and 2 of Gehrels (1986).

^c REFERENCES: (1) Imanishi & Terashima (2004); (2) Schartel et al. (2005); (3) Miller et al. (2006); (4) Grupe et al. (2003); (5) Page et al. (2011); (6) Braitto et al. (2004); (7) Ruiz et al. (2007); (8) Shemmer et al. (2005); (9) Ballo et al. (2011); (10) Schartel et al. (2010).

however, in cases where these regions were covering other X-ray sources, the background spectra were extracted from source-free circular regions with radii of $150''$ in the vicinity of the source. The numbers of counts in the source regions at energies of 0.5–2 keV are presented in Table 2. The RMFs used for spectral fitting were obtained from the public calibration database.¹⁰ The ARFs were generated with the PCARF routine; this routine does not include aperture corrections, and therefore the *ROSAT* fluxes were aperture-corrected using the integrated *ROSAT* PSPC PSF.

2.4. ASCA observations

For the *ASCA* observations of our sample we used XSELECT to extract the spectra from the previously processed clean events files publicly available in the Tartarus (Version 3.1) database.¹¹ We have extracted spectra from only the SIS cameras. This was based on the fact that the SIS cameras have a wider range of energy sensitivity and better angular resolution than the GIS proportional counters. For the SIS, the counts from each quasar were extracted from circular regions with aperture radii of $3.2'$. The background spectra for the SIS observations were extracted from source-free polygons covering most of the nominal chip at distance $> 4.2'$ from the source center. The background subtracted SIS count rates in the 0.6–9.5 keV band are presented in Table 4.

2.5. BeppoSAX and Einstein observations

For the *BeppoSAX* and *Einstein* observations of our sample we collected the count rates from already published works. The count rates for the *BeppoSAX* MECS observations were obtained from Braitto et al. (2004) in the case of Mrk 231 and from Brandt et al. (1999) in the case of CSO 755. The published count rates were extracted in the 1.8–10 keV band using circular regions with radii $2'$ and $3'$ for Mrk 231 and CSO 755, respectively. The count rates for the *Einstein* IPC observations of our sources were obtained from Wilkes et al. (1994). These count rates were extracted in the 0.16–3.5 keV band using circular regions with $3'$ radii. We used the Portable, Interactive Multi-Mission Simulator software (PIMMS; Mukai 1993) to derive X-ray fluxes from the published *BeppoSAX* and *Einstein* count rates.

2.6. New X-ray detection of IRAS 14026+4341

In this work we report for the first time an X-ray detection of IRAS 14026+4341, a highly polarized BAL quasar that has been studied in detail at other wavelengths (e.g., Boroson & Meyers 1992; Hines et al. 2001). We detect this source with a statistical significance of $\approx 4\sigma$ in the MOS2 observation performed on 2005 Nov 26, $\approx 3\sigma$ in the MOS1 observation performed on 2006 Jan 16, and $\approx 5\sigma$ in our new ACIS-S observation performed on 2010 Jul 28. The significances of the detections of IRAS 14026+4341 were calculated by estimating the Poisson probability of obtaining at least the observed number of counts based on the expected background. This probability provides a statistical test of the null hypothesis that the observed photon counts solely originate from the background. For the MOS2 observation

performed on 2005 Nov 26 there are 21 counts detected with a predicted background number of 6.63, and therefore the null probability is 6.6×10^{-6} ; i.e., we reject the null hypothesis with a significance of $\approx 4.4\sigma$. For the MOS1 observation performed on 2006 Jan 16 there are 19 counts detected with a predicted number of 7.45, and therefore the null probability is 2.8×10^{-4} (significance of $\approx 3.4\sigma$). For the *Chandra* observation there are 6 counts detected with a predicted background number of 0.22, and therefore the null probability is 1.3×10^{-7} (significance of $\approx 5.1\sigma$). The detections of IRAS 14026+4341 in the MOS cameras are close to the detection threshold, and therefore different choices of energy range and/or source and background extraction regions could result in a non-detection of the source as in the case of Ruiz et al. (2007). For the observations of IRAS 14026+4341 we have used our default annular background region. As an additional test of the detections of IRAS 14026+4341 in the MOS cameras, we select two $80''$ radius source-free circular regions in the vicinity of the source as the background. Using these background regions for the MOS2 observation performed on 2005 Nov 26, the predicted numbers of background counts are 7.98 and 9.66. Thus the detection significances are $\approx 3.7\sigma$ and $\approx 3.1\sigma$. For the MOS1 observation performed on 2006 Jan 16 the predicted numbers of background counts are 6.41 and 7.76; therefore the detection significances are $\approx 3.9\sigma$ and $\approx 3.3\sigma$. The detection of IRAS 14026+4341 in its *Chandra* observation has $\approx 5\sigma$ significance independent of the selection of the background region. For example, using as background regions two $20''$ radius source-free circular regions in the vicinity of the source, the expected numbers of background counts are 0.24 and 0.32. Thus, the detection significances are $\approx 5.1\sigma$ and $\approx 4.7\sigma$.

3. SPECTRAL ANALYSIS

The spectral analysis of our sample was undertaken with the main goal of searching for long-term flux variability within the set of X-ray observations of each source. Our objective is not to perform a detailed spectral modeling of each source in our sample but to obtain robust basic flux measurements. Spectral analysis was performed using XSPEC v.12.0; the fitting bands used were 0.5–8 keV for the *Chandra* observations, 0.5–10 keV for the *XMM-Newton* MOS observations, 0.3–10 keV for the *XMM-Newton* pn observations, 0.6–9.5 keV for the *ASCA* SIS observations, and 0.5–2 keV for the *ROSAT* PSPC observations. The spectral fits were performed in the full fitting band of each instrument using the C -statistic (Cash 1979). The C -statistic may not be appropriate to utilize when performing background subtraction. To use the C -statistic properly, we fit the background spectra with a flat response using the CPLINEAR model.¹² The background model is scaled and subtracted when we fit the source spectra.

For *Chandra* we performed fits using each of the new and archival observations. For *XMM-Newton* we performed fits using each of the EPIC cameras with detected spectra separately; we also performed joint fits using the three EPIC cameras together. The fits from each separate EPIC camera are consistent with the joint fits, and

¹⁰ <ftp://legacy.gsfc.nasa.gov>

¹¹ <http://tartarus.gsfc.nasa.gov>

¹² This model is included in the ACIS-EXTRACT package (Broos et al. 2010).

TABLE 4
LOG OF *ASCA* ARCHIVAL OBSERVATIONS

OBJECT NAME	OBS. DATE	EXP. TIME(KS) ^a		COUNT RATE($\times 10^3$)		REF. ^b
		SIS0	SIS1	SIS0	SIS1	
IRAS 07598+6508	1996 Oct 29	37.2	37.2	<2.3	<3.3	2
PG 0946+301	1998 Nov 12	70.1	64.8	1.3 \pm 0.5	<1.0	3
PG 1001+054	1999 Nov 12	38.0	40.1	<1.4	<1.3	1
Mrk 231	1994 Dec 05	19.4	18.2	9.9 \pm 1.2	7.4 \pm 1.2	2
Mrk 231	1999 Nov 10	86.4	90.0	11.2 \pm 0.6	9.1 \pm 0.5	4
PG 1700+518	1998 Mar 24	18.3	14.7	<2.1	<2.1	2
PG 2112+059	1999 Oct 30	31.1	28.4	20.2 \pm 1.2	13.3 \pm 1.0	5

NOTE. — The SIS count rates are for the 0.6–9.5 keV band extracted from a circular region of radius 3.2'. Count rate upper limits are at the 3σ significance level. The count rates and exposure times for all the observations with exception of the one of IRAS 07598+6508 have been obtained selecting source and background regions from the cleaned event files of the NASA Tartarus database (version 3.1; <http://astro.ic.ac.uk/Research/Tartarus>). The upper limits and exposure times for the observation of IRAS 07598+6508 have been obtained from Gallagher et al. (1999).

^a The exposure times and photon counts are obtained after screening the data.

^b REFERENCES: (1) this work; (2) Gallagher et al. (1999); (3) Mathur et al. (2000); (4) Maloney & Reynolds (2000) (5) Gallagher et al. (2001).

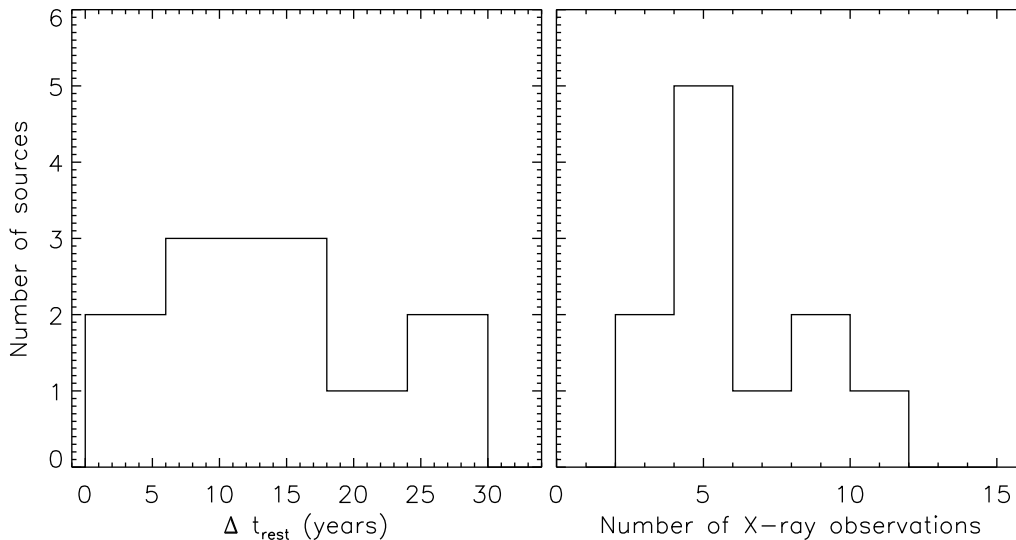


FIG. 1.— Number of sources versus rest-frame time span of X-ray coverage (left panel) and number of X-ray observations (right panel).

therefore we present only the joint fits in this work. The same conclusion was obtained for the *ASCA* SIS cameras, and therefore we present only the joint fits of the SIS0 and SIS1 cameras in this work.

For deriving fluxes and luminosities of each source we used a simple power-law model including intrinsic absorption in the cases where significant absorption was found ($> 99\%$ level of significance); in all cases we included Galactic absorption from Dickey & Lockman (1990). Galactic absorption column densities (from Dickey & Lockman 1990) were obtained at the optical coordinates of the sources (see Tables 1 and 2) through the use of the HEASARC N_{H} tool.¹³ The power-law photon index (Γ) was free to vary for those *Chandra*, *XMM-Newton*, and *ASCA* observations where the signal-to-noise ratio (S/N) of the observation was greater than seven. The value of S/N is estimated from the total

number of counts divided by the average of the upper and lower error bars; the total photon counts with their error bars are found in Tables 2, 3 and 4. In the cases where $S/N \leq 7$ and for the *ROSAT* observations,¹⁴ we fixed the photon index to the weighted average if there are other observations of the source with $S/N > 7$ or otherwise to 1.8. It is important to emphasize that we are not correcting for intrinsic absorption when we derive fluxes. This allows us to make reliable estimations of the absorbed fluxes and luminosities regardless of the model that we are using since these quantities are rather insensitive to spectral model choice. Given the low S/N of most of the spectra analyzed in this work, a simple or absorbed power-law gives an acceptable fit for almost every observation; however, in a few cases of high S/N

¹⁴ The 0.5–2 keV band observations with *ROSAT* cannot be used to give a reliable estimation of the full-band (0.5–8 keV) photon index.

¹³ <http://heasarc.gsfc.nasa.gov/cgi-bin/Tools/w3nh/w3nh.pl>

TABLE 5
BEST-FIT POWER-LAW X-RAY SPECTRAL PARAMETERS

OBJECT NAME	OBS. DATE	N_{H}^{a} (10^{22} cm^{-2})	Γ	C -stat(DOF)	Instrument
IRAS 07598+6508	1991 Mar 17	<0.15	2.71	22.0(22)	PSPC
	2000 Mar 21	<0.52	2.71	7.0(8)	ACIS-S
	2001 Oct 24	<0.06	2.71 ± 0.19	301.3(345)	EPIC
	2010 Jun 18	<0.12	2.71	36.4(27)	ACIS-S
PG 0946+301	1998 Nov 12	12_{-6}^{+10}	1.48	303.7(321)	SIS
	2010 Jan 11	$7.3_{-5.3}^{+7.1}$	1.48 ± 0.86	58.2(52)	ACIS-S
PG 1001+054	1992 May 17	<0.19	2.04	11.5(9)	PSPC
	2003 May 04	<0.01	2.04 ± 0.15	557.0(325)	EPIC
	2010 Jan 11	<0.27	2.04	4.3(11)	ACIS-S
PG 1004+130	2003 May 04	<0.01	1.39 ± 0.04	1204.4(1339)	EPIC
	2005 Jan 05	<0.15	1.03 ± 0.06	521.8(545)	ACIS-S
Q 1246-057	1991 Dec 21	<8.1	1.58	22.3(28)	PSPC
	1993 Jan 05	<3.6	1.58	15.5(12)	PSPC
	1993 Jun 22	<2.6	1.58	39.0(66)	PSPC
	2000 Feb 08	$3.8_{-2.8}^{+3.5}$	1.58	26.4(36)	ACIS-S
	2001 Jul 11	$0.67_{-0.55}^{+0.69}$	1.83 ± 0.20	441.8(584)	EPIC
	2004 Jul 15	<1.2	1.40 ± 0.17	542.9(606)	EPIC
Mrk 231	1991 Jun 7	<0.01	1.03	121.4(103)	PSPC
	1994 Dec 05	<0.10	1.00 ± 0.22	251.4(304)	SIS
	1999 Nov 10	<0.02	0.94 ± 0.10	814.8(882)	SIS
	2000 Oct 19	<0.00	1.03 ± 0.06	731.8(629)	ACIS-S
	2001 Jun 07	<0.00	1.06 ± 0.04	1919.7(1663)	EPIC
	2003 Feb 03	<0.00	1.07 ± 0.06	719.9(603)	ACIS-S
	2003 Feb 11	<0.00	1.05 ± 0.06	847.9(582)	ACIS-S
	2003 Feb 20	<0.00	0.95 ± 0.07	694.0(605)	ACIS-S
	2010 Jul 11	<0.03	0.89 ± 0.20	189.2(211)	ACIS-S
IRAS 14026+4341	2005 Nov 26	<4.5	1.80	24.2(18)	EPIC
	2006 Jan 16	<1.5	1.80	30.3(18)	EPIC
	2010 Jul 28	<113	1.80	8.6(5)	ACIS-S
CSO 755	2001 Jul 30	<3.4	$1.50_{-0.32}^{+0.42}$	47.8(63)	EPIC
	2001 Dec 08	1.20 ± 0.30	1.83 ± 0.07	1036.9(1161)	EPIC
	2001 Dec 13	$2.8_{-1.5}^{+1.9}$	2.02 ± 0.29	213.1(238)	EPIC
	2010 Mar 21	<5.3	1.97 ± 0.46	79.0(82)	ACIS-S
SBS 1542+541	1993 Ago 14	<4.5	1.74	13.5(24)	PSPC
	2000 Mar 22	<4.0	1.55 ± 0.49	56.6(65)	ACIS-S
	2002 Feb 03	<1.6	1.73 ± 0.26	214.7(254)	EPIC
	2002 Feb 06	$0.52_{-0.37}^{+0.41}$	1.76 ± 0.13	576.9(647)	EPIC
PG 1700+518	2009 Dec 19	<0.04	1.77	49.2(44)	EPIC
	2009 Dec 31	<0.08	1.77	141.2(124)	EPIC
	2010 Jan 02	<0.12	$1.77_{-0.30}^{+0.33}$	191.0(195)	EPIC
	2010 Jun 26	<0.11	1.77	19.0(13)	ACIS-S
PG 2112+059	1991 Nov 30	<0.20	0.91	39.9(46)	PSPC
	1999 Oct 30	1.14 ± 0.50	1.91 ± 0.26	506.1(599)	SIS
	2002 Sep 01	<0.03	0.84 ± 0.09	390.8(399)	ACIS-S
	2003 May 14	<0.02	1.59 ± 0.06	896.1(958)	EPIC
	2005 Nov 20	<0.00	0.84 ± 0.08	1095.1(1023)	EPIC
	2007 May 03	<0.02	0.66 ± 0.11	583.6(585)	EPIC
	2007 May 19	<0.01	0.69 ± 0.07	1053.0(1164)	EPIC
	2007 May 21	<0.01	0.62 ± 0.06	1495.4(1509)	EPIC
	2007 Nov 05	<0.02	0.58 ± 0.09	779.6(891)	EPIC

NOTE. — The best-fit column densities were obtained from a power-law model with intrinsic absorption at the redshift of the source. The same model was used to estimate the best-fit photon index and C -statistic for the observations of PG 0946+301, Q 1246-057, SBS 1542+541, CSO 755, and PG 2112+059. The best-fit photon index and C -statistic for all the other observations were obtained from an unabsorbed power-law model. In all the fits we have assumed Galactic absorption with column densities obtained from Dickey & Lockman (1990). Errors and upper limits represent 90% confidence intervals for each value, taking one parameter to be of interest ($\Delta C=2.71$; e.g., Avni 1976).

^a Intrinsic neutral hydrogen column density in units of 10^{22} cm^{-2} .

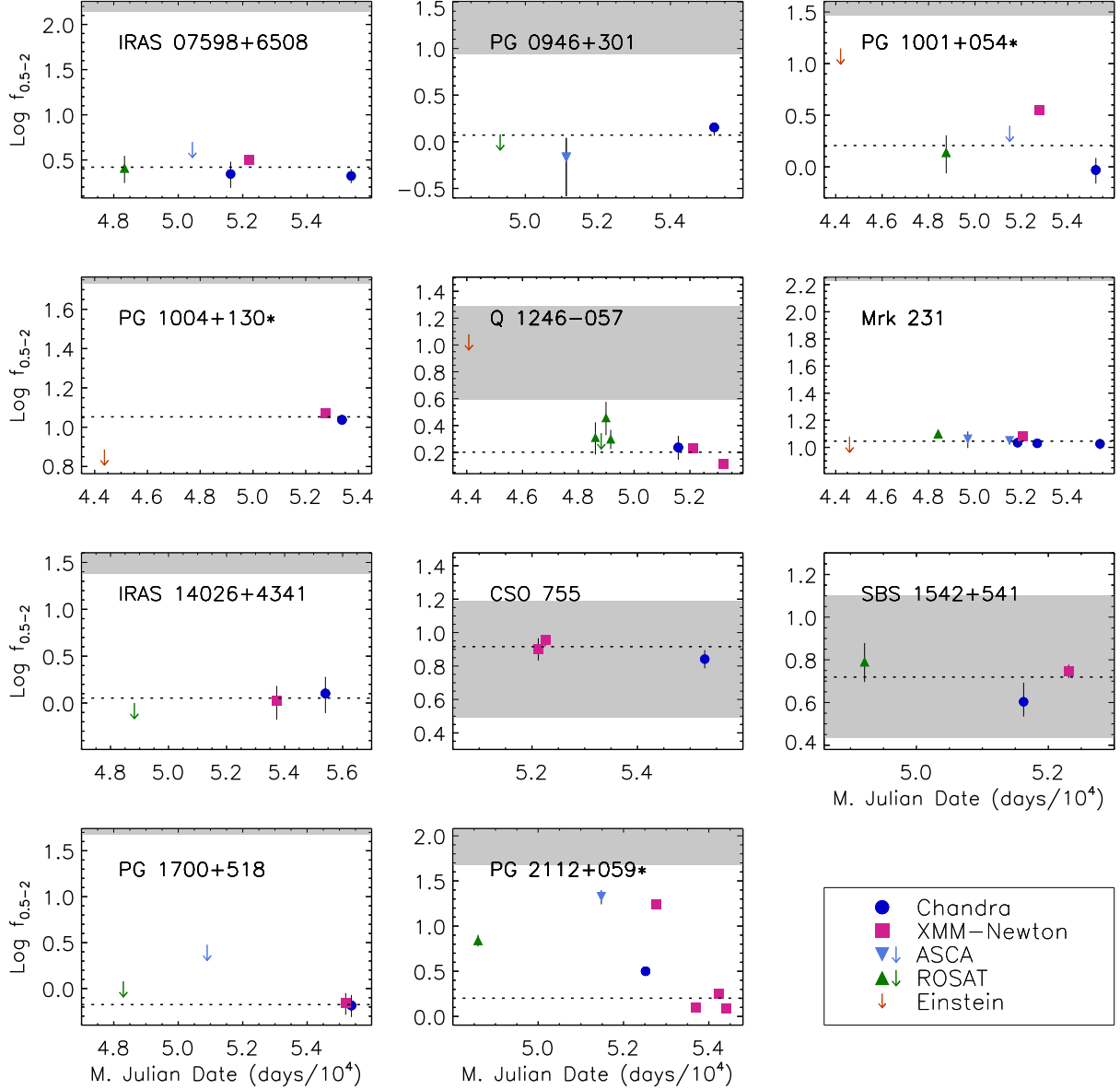


FIG. 2.— Logarithm of the observed flux in the 0.5–2 keV band (in units of $10^{-14} \text{ erg cm}^{-2} \text{ s}^{-1}$) versus modified Julian date for the BAL quasars in our sample. The circles, squares, inverted triangles, and triangles indicate observations performed with *Chandra*, *XMM-Newton*, *ASCA*, and *ROSAT*, respectively. Given that Mrk 231 did not present variability in the set of *Chandra* observations performed in 2003, for visualization purposes we have plotted these observations as a single point with their mean flux and a typical error bar. The same procedure has been applied to the *XMM-Newton* observations of IRAS 14026+4341, the *XMM-Newton* observations of CSO 755 performed in 2001 Dec, the *XMM-Newton* observations of SBS 1542+541, the *XMM-Newton* observations of PG 1700+518, and the *XMM-Newton* observations of PG 2112+059 performed in 2007 May. The upper limits at early times found in the panels of PG 1001+054, PG 1004+130, Q 1246-057, and Mrk 231 correspond to the *Einstein* observations. The shaded areas in each panel correspond to the expected range of X-ray fluxes obtained assuming a typical α_{OX} (see Table 5 of Steffen et al. 2006) and a power-law spectrum with $\Gamma = 1.9$. The sources marked with * present evidence of variability in at least one of the energy bands considered. The horizontal dotted lines correspond to the best-fit constant flux.

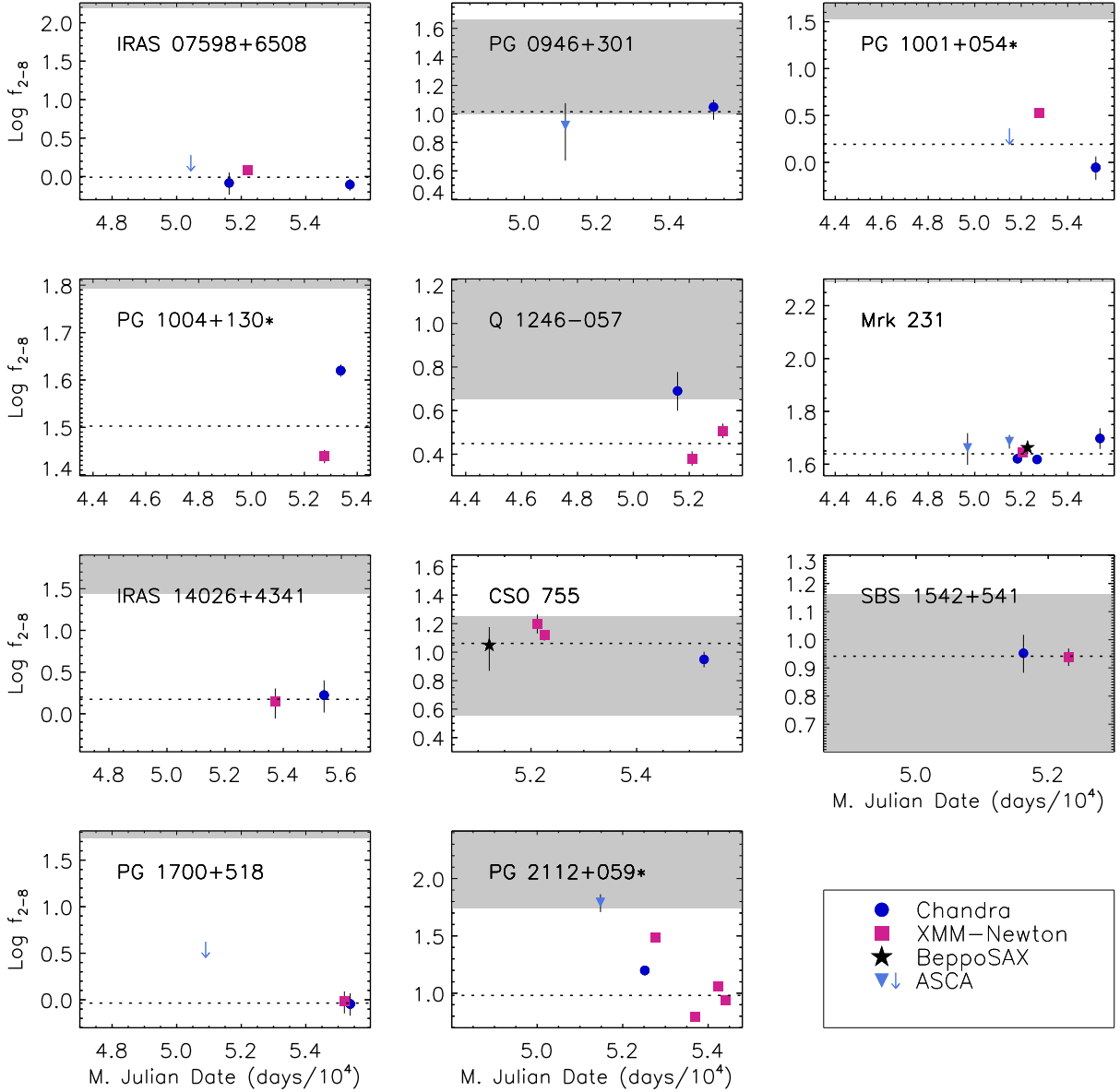


FIG. 3.— Logarithm of the observed flux in the 2–8 keV band (in units of 10^{-14} erg cm^{-2} s^{-1}) versus modified Julian date for the BAL quasars in our sample. The circles, squares, stars and inverted triangles indicate observations performed with *Chandra*, *XMM-Newton*, *BeppoSAX*, and *ASCA*, respectively. See the Figure 2 caption for additional details about the presentation.

($S/N > 25$) where we find evidence of complexity in the spectra, we also estimate fluxes and luminosities using more complex models (see §4.2).

The best-fitted parameters using a power-law model are presented in Table 5. There are five sources that presented evidence of absorption in their spectra; these sources are PG 0946+301, Q 1246–057, CSO 755, SBS 1542+541, and PG 2112+059 (see Table 5). PG 0946+301 shows in both *Chandra* and *ASCA* observations moderate-to-strong absorption with column densities $\sim 10^{23}$ cm^{-2} . This source presents moderate and low S/N in its *Chandra* and *ASCA* observations, respectively. Therefore, new *Chandra* and/or *XMM-Newton* observations with exposures $\gtrsim 20$ ks are needed in order to better constrain the absorption found in PG 0946+301. Q 1246–057 shows moderate intrinsic absorption ($N_{\text{H}} \sim 10^{22}$ cm^{-2}) as we confirm in the *Chandra* observation performed in 2000 and the

XMM-Newton observation performed in 2001 (first studied by Grupe et al. 2003). CSO 755 presents moderate intrinsic absorption ($N_{\text{H}} \sim 10^{22}$ cm^{-2}) as we confirm in the *XMM-Newton* observations (first studied by Shemmer et al. 2005). SBS 1542+541 shows low intrinsic absorption ($N_{\text{H}} \lesssim 10^{22}$ cm^{-2}) as we confirm in the last *XMM-Newton* observation performed in 2002 (first studied by Grupe et al. 2003). PG 2112+059 presents evidence of moderate absorption only in its *ASCA* observation performed in October 1999 (first studied by Gallagher et al. 2001); however, the flat measured power laws in other observations suggest absorption is likely present.

The derived X-ray fluxes in the 0.5–2 keV, 2–8 keV, and 0.5–8 keV bands from simple or absorbed power-law fits are presented in Table 6 and Figures 2, 3, and 4. There we have also presented fluxes from observations with *BeppoSAX* and *Einstein*; these fluxes were ob-

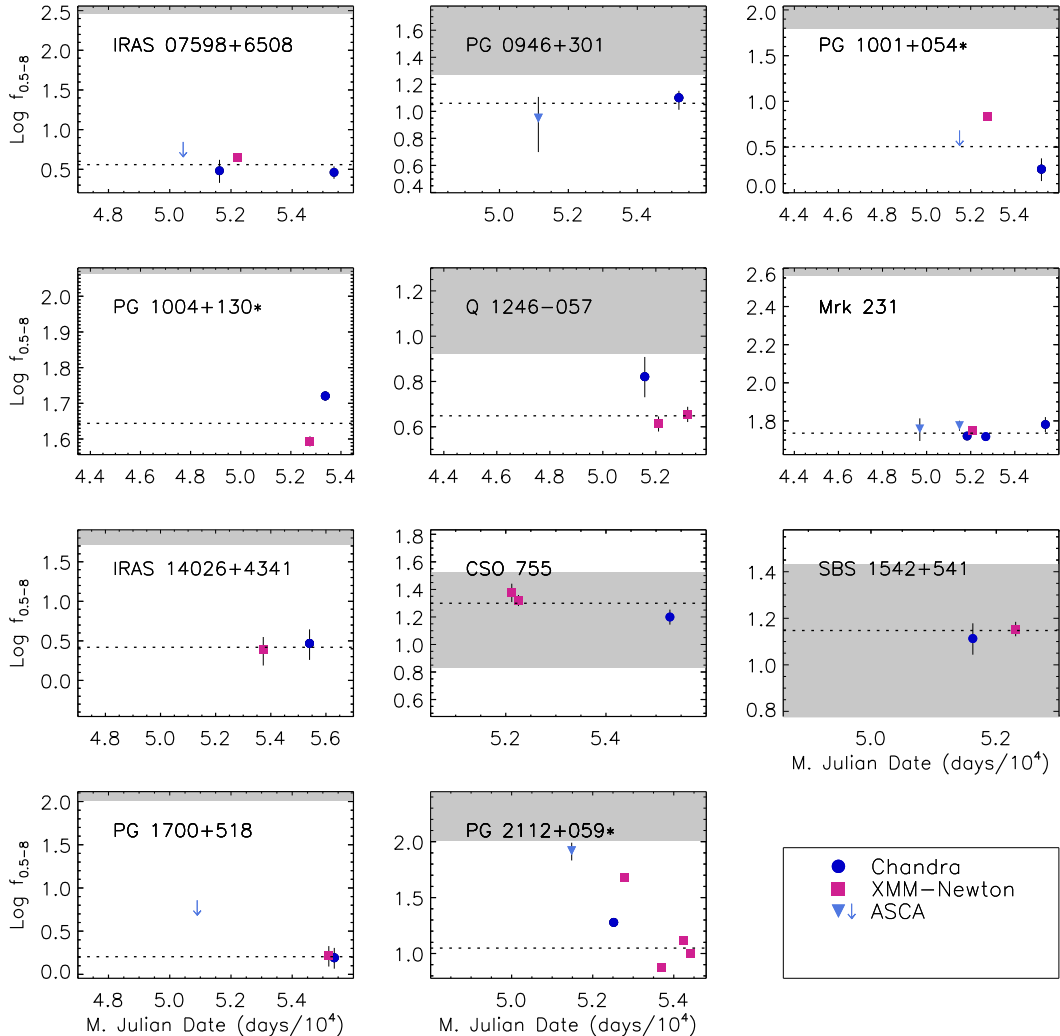


FIG. 4.— Logarithm of the observed flux in the 0.5–8 keV band (in units of 10^{-14} erg cm $^{-2}$ s $^{-1}$) versus modified Julian date for the BAL quasars in our sample. The circles, squares, and inverted triangles indicate observations performed with *Chandra*, *XMM-Newton*, and *ASCA*, respectively. See the Figure 2 caption for additional details about the presentation.

tained from published count rates using the PIMMS tool (see §2). We assumed power-law spectra with the average parameters (Γ and N_{H}) taken from spectral fits of the high S/N observations of each source. The error bars for the *BeppoSAX* MECS observations were obtained by propagating the uncertainties on the instrumental background¹⁵ and source count rates presented in Brandt et al. (1999) and Braito et al. (2004). The *Einstein* observations of our sources provided only upper limits. We confirmed that the estimates of *Einstein* fluxes with PIMMS give a reliable result by comparing our values with those of Wilkes et al. (1994); in general the differences are less than 10%. Similarly, our *BeppoSAX* fluxes are consistent within 10% with those of Brandt et al. (1999) and Braito et al. (2004).

Note that we have only estimated fluxes and luminosities in the bands where the instruments are sensitive. Therefore, in the case of the *ROSAT* PSPC and *Einstein* IPC observations we only present fluxes in the 0.5–2 keV band, and in the case of the *BeppoSAX* MECS we only

present fluxes in the 2–8 keV band.

4. RESULTS AND DISCUSSION

In this section we describe the main results found in the X-ray variability study of our BAL quasar sample. In §4.1 we constrain variability using simple power-law models (as described in §3) to estimate fluxes; in §4.2 we constrain variability using more complex models to estimate fluxes; finally, in §4.3 we examine possible physical scenarios to explain the results found.

4.1. Long and short-term variability

Long-term variability was assessed initially by comparing the fluxes in the 0.5–2 keV, 2–8 keV, and 0.5–8 keV bands for all the detections of each source. In order to test the significance of any variability, we calculate for each source the χ^2 statistic where the data points are the fluxes of each observation (with their respective 1σ errors) and the model is the best-fit constant flux. The χ^2 value provides a statistical test of the null hypothesis that the flux of each epoch is equal to the best-fit flux (average flux weighted by errors) of all the observations.

In Table 7 we list the best-fit constant fluxes for each source in each band. In this table we also have

¹⁵ To estimate the background count rates we used the background files found at the NASA HEASARC site (http://heasarc.nasa.gov/docs/sax/archive/calibration_files.html).

TABLE 6
DERIVED X-RAY FLUXES FROM POWER-LAW FITS

OBJECT NAME ^a	OBS. DATE	$f_{0.5-2}$ ^b	f_{2-8} ^b	$f_{0.5-8}$ ^b	$f_{2\text{keV}}$ ^c	Instrument
IRAS 07598+6508	1991 Mar 17	2.60±0.89	2.88±0.99	PSPC
	1996 Dec 21	<5.0	<1.9	<7.0	<5.6	SIS
	2000 Mar 21	2.21 ^{+0.82} _{-0.66}	0.83 ^{+0.31} _{-0.25}	3.03 ^{+1.13} _{-0.90}	2.45 ^{+0.91} _{-0.73}	ACIS-S
	2001 Oct 24	3.20±0.29	1.20±0.11	4.40±0.39	3.55±0.32	EPIC
PG 0946+301	2010 Jun 18	2.10±0.38	0.79±0.14	2.89±0.52	2.33±0.42	ACIS-S
	1993 Nov 14	<1.2	<0.8	PSPC
	1998 Nov 12	0.68±0.42	8.3±3.6	8.9±3.9	<0.6	SIS
	2010 Jan 11	1.43 ^{+0.18} _{-0.27}	11.2 ^{+1.4} _{-2.1}	12.6 ^{+1.6} _{-2.3}	0.69±0.11	ACIS-S
PG 1001+054*	1979 Dec 02	<14	<24	IPC
	1992 May 17	1.40 ^{+0.64} _{-0.52}	2.4 ^{+1.1} _{-0.9}	PSPC
	1999 Nov 12	<2.5	<2.3	<4.8	<4.2	SIS
	2003 May 04	3.53±0.36	3.35±0.34	6.88±0.70	5.99±0.61	EPIC
	2010 Jan 11	0.93±0.27	0.88±0.25	1.81±0.52	1.58±0.45	ACIS-S
PG 1004+130*	1980 May 09	<7.7	<20	IPC
	2003 May 04	11.76±0.38	27.45±0.89	39.2±1.3	28.27±0.92	EPIC
	2005 Jan 05	10.90±0.32	41.7±1.2	52.6±1.6	29.72±0.88	ACIS-S
Q 1246-057	1979 Jul 20	<12	<38	IPC
	1991 Dec 21	2.07±0.57	4.4±1.2	PSPC
	1992 Jul 17	<2.2	<6.2	PSPC
	1993 Jan 05	3.18±0.91	12.5±3.6	PSPC
	1993 Jun 22	2.21±0.36	7.5±1.2	PSPC
	2000 Feb 08	1.73±0.35	4.9±1.0	6.6±1.4	1.97±0.41	ACIS-S
	2001 Jul 11	1.70±0.13	2.40±0.18	4.10±0.31	6.28±0.48	EPIC
	2004 Jul 15	1.30±0.10	3.22±0.25	4.52±0.35	3.94±0.30	EPIC
Mrk 231	1980 Dec 23	<12	<33	IPC
	1991 Jun 07	12.73±0.93	34.6±2.5	PSPC
	1994 Dec 05	11.5±1.6	45.9±6.3	57.3±7.8	31.6±4.3	SIS
	1999 Nov 10	11.2±0.67	48.5±2.9	59.6±3.6	31.7±1.9	SIS
	2000 Oct 19	10.83±0.34	41.7±1.3	52.6±1.7	29.48±0.93	ACIS-S
	2001 Jun 07	12.07±0.35	44.3±1.3	56.3±1.6	32.26±0.94	EPIC
	2001 Dec 29	...	46.0±2.5	MECS
	2003 Feb 03	10.98±0.33	39.7±1.2	50.7±1.6	29.21±0.89	ACIS-S
	2003 Feb 11	10.88±0.34	40.7±1.3	51.6±1.6	29.29±0.91	ACIS-S
	2003 Feb 20	10.29±0.33	44.1±1.4	54.4±1.8	29.09±0.95	ACIS-S
	2010 Jul 11	10.62±0.96	49.8±4.5	60.5±5.5	40.0±2.8	ACIS-S
IRAS 14026+4341	1992 Jul 18	<1.0	<2.1	PSPC
	2005 Nov 26	1.28±0.44	1.69±0.58	3.0±1.0	2.73±0.94	EPIC
	2006 Jan 16	0.84±0.42	1.11±0.55	1.95±0.97	1.79±0.89	EPIC
	2010 Jul 28	1.27 ^{+0.64} _{-0.48}	1.67 ^{+0.84} _{-0.64}	2.9 ^{+1.5} _{-1.1}	2.7 ^{+1.4} _{-1.0}	ACIS-S
CSO 755	1999 Feb 02	...	11.2±3.8	MECS
	2001 Jul 30	8.0±1.2	15.8±2.4	23.7±3.7	32.5±5.0	EPIC
	2001 Dec 08	9.09±0.29	13.10±0.42	22.18±0.71	31.1±1.0	EPIC
	2001 Dec 13	8.48±0.84	11.1±1.1	19.6±1.9	18.8±1.9	EPIC
	2010 Mar 21	6.94±0.87	8.9±1.1	15.8±2.0	20.5±2.6	ACIS-S
SBS 1542+541	1993 Ago 14	6.2±1.3	15.4±3.2	PSPC
	2000 Mar 22	4.01±0.62	9.0±1.4	13.0±2.0	10.3±1.6	ACIS-S
	2002 Feb 03	5.34±0.50	8.55±0.80	13.9±1.3	19.6±1.8	EPIC
	2002 Feb 06	5.81±0.29	8.79±0.44	14.60±0.73	22.1±1.1	EPIC
PG 1700+518	1991 Feb 09	<1.2	<2.5	PSPC
	1998 Mar 24	<3.0	<4.2	<7.2	<6.4	SIS
	2009 Dec 19	0.83±0.19	1.15±0.26	1.98±0.45	1.77±0.40	EPIC
	2009 Dec 31	0.50±0.14	0.68±0.20	1.18±0.34	1.06±0.30	EPIC
	2010 Jan 02	0.76±0.16	1.04±0.21	1.80±0.37	1.61±0.33	EPIC
	2010 Jun 26	0.66±0.18	0.90±0.25	1.56±0.43	1.39±0.38	ACIS-S
PG 2112+059*	1991 Nov 30	7.0±1.0	19.6±2.9	PSPC
	1999 Oct 30	21.2±3.8	62±11	83±15	77±14	SIS
	2002 Sep 01	3.17±0.14	15.81±0.69	18.98±0.83	8.94±0.39	ACIS-S
	2003 May 14	17.35±0.74	30.8±1.3	48.1±2.1	42.6±1.8	EPIC
	2005 Nov 20	1.25±0.07	6.26±0.34	7.51±0.40	3.54±0.19	EPIC
	2007 May 03	1.88±0.13	11.98±0.86	13.86±0.99	5.42±0.39	EPIC
	2007 May 19	1.67±0.08	10.26±0.47	11.93±0.55	4.81±0.22	EPIC
	2007 May 21	1.74±0.06	11.86±0.44	13.60±0.51	5.04±0.19	EPIC
	2007 Nov 05	1.21±0.07	8.73±0.52	9.94±0.59	3.53±0.21	EPIC

NOTE. — Fluxes are obtained from the best-fitting parameters for a simple power-law model (most cases) or an intrinsic absorbed power-law model (for observations as indicated in the previous table). In both cases, fixed Galactic absorption was also included. The fluxes are not corrected for intrinsic absorption.

^a The sources marked with * present evidence of variability in at least one of the energy bands considered.

^b Observed fluxes in the 0.5–2, 2–8, and 0.5–8 keV bands in units of 10^{-14} erg cm⁻² s⁻¹.

^c Observed flux densities at rest-frame 2 keV in units of 10^{-32} erg cm⁻² s⁻¹ Hz⁻¹.

TABLE 7
TESTS FOR VARIABILITY: CONSTANT FLUX FITS

OBJECT NAME	Fluxes [10^{-14} erg cm $^{-2}$ s $^{-1}$] ^a			χ^2 /DOF			% SIGNIFICANCE		
	0.5–2 keV	2–8 keV	0.5–8 keV	0.5–2 keV	2–8 keV	0.5–8 keV	0.5–2 keV	2–8 keV	0.5–8 keV
POWER-LAW FITS									
IRAS 07598+6508	2.79	1.05	3.84	5.6/3	5.7/2	5.6/2	86.8	94.3	93.9
PG 0946+301	1.21	10.46	11.63	2.3/1	0.5/1	0.7/1	86.9	50.8	58.1
PG 1001+054	1.93	1.89	3.89	33.4/2	32.8/1	32.7/1	>99.9	>99.9	>99.9
PG 1004+130	11.27	32.50	44.74	3.0/1	87.7/1	44.2/1	91.5	>99.9	>99.9
Q 1246–057	1.54	2.76	4.38	15.7/5	12.5/2	4.2/2	99.2	99.8	87.5
Mrk 231	11.05	42.56	53.45	18.1/8	20.0/8	13.1/7	98.0	99.0	93.0
IRAS 14026+4341	1.14	1.50	2.63	0.6/2	0.6/2	0.6/2	26.4	26.4	26.4
CSO 755	8.82	12.54	21.42	5.7/3	15.2/4	9.6/3	87.2	99.6	97.8
SBS 1542+541	5.51	8.75	14.32	6.8/3	0.1/2	0.7/2	92.4	4.3	28.1
PG 1700+518	0.68	0.93	1.61	2.5/3	2.5/3	2.5/3	53.1	52.8	52.9
PG 2112+059	1.64	10.07	11.72	717.0/8	504.9/7	560.1/7	>99.9	>99.9	>99.9
POWER-LAW FITS WITH CROSS-CALIBRATION UNCERTAINTIES									
IRAS 07598+6508	2.63	0.98	3.62	3.4/3	3.5/2	3.4/2	66.5	82.5	81.9
PG 0946+301	1.18	10.35	11.47	2.1/1	0.4/1	0.6/1	84.9	48.6	55.6
PG 1001+054	1.61	1.56	3.20	20.0/2	19.9/1	19.9/1	>99.9	>99.9	>99.9
PG 1004+130	11.29	31.82	44.05	0.3/1	7.4/1	3.8/1	38.9	99.4	94.9
Q 1246–057	1.59	2.81	4.45	9.5/5	6.8/2	2.8/2	91.1	96.7	75.8
Mrk 231	11.11	43.58	54.39	2.5/8	3.5/8	2.2/7	3.9	9.9	5.2
IRAS 14026+4341	1.13	1.49	2.62	0.6/2	0.6/2	0.6/2	25.3	25.3	25.3
CSO 755	8.24	11.52	19.92	2.1/3	7.0/4	4.2/3	45.7	86.4	76.4
SBS 1542+541	5.24	8.74	14.04	3.9/3	0.1/2	0.3/2	72.9	2.2	14.4
PG 1700+518	0.67	0.92	1.60	2.2/3	2.1/3	2.2/3	46.2	45.9	46.0
PG 2112+059	1.59	9.58	11.18	146.0/8	99.5/7	107.1/7	>99.9	>99.9	>99.9
POWER-LAW FITS WITH CROSS-CALIBRATION UNCERTAINTIES AND UPPER LIMITS									
IRAS 07598+6508	2.62	0.98	3.61	3.4/4	3.5/3	3.4/3	50.7	67.8	66.9
PG 0946+301	1.00	3.8/2	85.0
PG 1001+054	1.59	1.51	3.12	21.8/4	20.2/2	20.1/2	>99.9	>99.9	>99.9
PG 1004+130	10.45	9.2/2	99.0
Q 1246–057	1.58	11.5/7	88.4
Mrk 231	11.04	4.4/9	12.0
IRAS 14026+4341	0.86	3.0/3	61.4
PG 1700+518	0.68	0.94	1.62	3.0/5	3.0/4	3.0/4	30.5	44.1	44.0
FITS USING COMPLEX MODELS WITH CROSS-CALIBRATION UNCERTAINTIES									
Mrk 231	10.63	48.40	59.13	4.0/8	1.2/7	1.1/7	14.7	0.9	0.8
CSO 755	8.60	11.14	19.80	1.0/3	3.1/3	2.0/3	20.1	63.4	42.8
PG 2112+059	1.39	10.53	11.91	108.1/8	72.6/7	81.6/7	>99.9	>99.9	>99.9

^a Best-fitting constant flux (weighted average) from the *Chandra*, *XMM-Newton*, *BeppoSAX*, *ASCA*, and *ROSAT* detections of each source.

TABLE 8
AVERAGE S/N, EXPECTED FRACTION OF VARIABLE SOURCES, AND OBSERVED
MINIMUM-TO-MAXIMUM FLUX RATIOS.

OBJECT NAME ^a	$\langle S/N \rangle$	E.C. ^b	P_{VD} ^c	$\left[\frac{f_{\max}}{f_{\min}} \right]_{0.5-2}$	$\left[\frac{f_{\max}}{f_{\min}} \right]_{2-8}$	$\left[\frac{f_{\max}}{f_{\min}} \right]_{0.5-8}$
IRAS 07598+6508	6.6	50	0.20	1.5±0.4	1.5±0.4	1.5±0.4
PG 0946+301	4.7	27	0.20	2.1±1.4	1.4±0.7	1.4±0.7
PG 1001+054*	7.8	69	0.20	3.8±1.3	3.8±1.3	3.8±1.3
PG 1004+130*	45.1	2079	0.80	1.1±0.2	1.5±0.2	1.3±0.2
Q 1246–057	8.8	86	0.20	2.4±0.8	2.0±0.5	1.6±0.4
Mrk 231	29.8	917	0.43	1.2±0.2	1.3±0.2	1.2±0.2
IRAS 14026+4341	2.1	7	0.02	1.5±1.0	1.5±1.0	1.5±1.0
CSO 755	17.2	313	0.43	1.3±0.3	1.8±0.4	1.5±0.4
SBS 1542+541	13.4	193	0.43	1.6±0.5	1.1±0.2	1.1±0.2
PG 1700+518	4.8	28	0.20	1.7±0.7	1.7±0.7	1.7±0.7
PG 2112+059*	25.2	660	0.43	17.5±4.1	9.9±2.3	11.1±2.6

^a The sources marked with * present evidence of variability in at least one of the energy bands considered.

^b Expected number of counts in the *Chandra* full band in order to achieve the average S/N of the set of observations of each source.

^c Variability detection probabilities obtained from the expected mean number of counts in the *Chandra* full band. These probabilities are obtained from column 3 of this table and from Tables 1 and 3 of Gibson & Brandt (2012).

TABLE 9
DERIVED X-RAY FLUXES FROM COMPLEX MODELS FITS

OBJECT NAME ^a	OBS. DATE	$f_{0.5-2}$ ^b	f_{2-8} ^b	$f_{0.5-8}$ ^b	$f_{2\text{keV}}$ ^c	Instrument
Mrk 231	1991 Jun 07	11.0±1.6	14.8±3.9	PSPC
	1994 May 12	10.8±1.7	46.0±7.2	56.8±9.0	34.7±5.5	SIS
	1999 Nov 10	13.8±1.5	49.1±5.4	62.9±6.9	23.7±2.6	SIS
	2000 Oct 19	10.4±1.1	48.9±5.2	59.4±6.4	20.5±2.2	ACIS-S
	2001 Jun 07	11.5±0.5	51.9±2.3	63.4±2.8	17.88±0.79	EPIC
	2003 Feb 03	10.22±0.66	44.1±2.8	54.3±3.5	18.3±1.2	ACIS-S
	2003 Feb 11	10.13±0.60	48.8±2.9	58.9±3.5	14.93±0.89	ACIS-S
	2003 Feb 20	9.60±0.66	49.6±3.4	59.2±4.1	15.2±1.1	ACIS-S
	2010 Jul 11	10.3 ^{+2.1} _{-1.5}	49 ⁺¹⁰ ₋₇	59 ⁺¹² ₋₉	23.5 ^{+4.9} _{-3.5}	ACIS-S
CSO 755	2001 Jul 30	8.5±1.7	12.5±2.6	21.0±4.3	26.7±5.5	EPIC
	2001 Dec 08	9.14±0.43	12.46±0.59	21.6±1.0	27.4±1.3	EPIC
	2001 Dec 13	8.6±1.2	10.4±1.4	19.0±2.6	17.4±2.4	EPIC
	2010 Mar 21	7.1±1.6	8.3±1.9	15.4±3.5	22.3±5.1	ACIS-S
PG 2112+059*	1991 Nov 30	8.3 ^{+5.7} _{-3.5}	16 ⁺¹³ ₋₉	PSPC
	1999 Oct 30	31.3±4.2	63.8±8.6	95±13	75±10	SIS
	2002 Sep 01	3.06±0.32	14.7±1.5	17.7±1.8	7.14±0.74	ACIS-S
	2003 May 14	16.3±1.3	34.7±2.7	51.0±3.9	41.2±3.2	EPIC
	2005 Nov 20	1.13±0.08	7.54±0.56	8.67±0.64	2.20±0.16	EPIC
	2007 May 03	1.62±0.22	12.6±1.7	14.2±1.9	3.67±0.50	EPIC
	2007 May 19	1.54±0.18	10.7±1.2	12.3±1.4	4.06±0.46	EPIC
	2007 May 21	1.44±0.11	12.38±0.91	13.8±1.0	3.62±0.26	EPIC
	2007 Nov 05	1.12±0.13	9.1±1.1	10.2±1.2	3.02±0.36	EPIC

NOTE. — Fluxes are obtained from the best-fitting parameters of the ionized-absorbed power-law model for CSO 755 and the thermal plasma + two absorbed power-laws model in the case of Mrk 231 and PG 2112+059. The fluxes are not corrected for intrinsic absorption.

^a The sources marked with * present evidence of variability in at least one of the energy bands considered.

^b Observed fluxes in the 0.5–2, 2–8, and 0.5–8 keV bands in units of 10^{-14} erg cm⁻² s⁻¹.

^c Observed flux densities at rest-frame 2 keV in units of 10^{-32} erg cm⁻² s⁻¹ Hz⁻¹.

listed the values of χ^2 for our model to test variability. We find that six out of eleven sources show evidence for variability (significance > 99%; see Table 7). The sources with potential variability are PG 1001+054, PG 1004+130, Q 1246–057, Mrk 231, CSO 755, and PG 2112+059. Notice that for most of these sources the apparent variability is found between observations performed with different X-ray instruments (e.g., see Figures 2, 3, and 4). The only exception is PG 2112+059 where variability is independently found in the *XMM-Newton* observations (see Figures 2, 3, 4

and Table 6). Therefore, in order to assess the variability reliably we must take into account uncertainties associated with cross calibration between the different X-ray missions used in this work. From studies of different astrophysical sources that can be considered “standard candles” in the X-ray regime the main conclusion is that, in general, the cross-calibration errors in the X-ray fluxes between *Chandra*, *XMM-Newton*, *BeppoSAX*, *ASCA*, *ROSAT*, and *Einstein* should be $\lesssim 10\%$ (e.g., Snowden 2002; Kirsch et al. 2005; Nevalainen et al. 2010; Weisskopf et al. 2010; Tsujimoto et al. 2011). Therefore,

as a second test of the variability found we add in quadrature to the error bars of each measured flux a 10% error. The new constant flux estimates with their χ^2 values and significances are presented in Table 7. We find that three (PG 1001+054, PG 1004+130, and PG 2112+059) out of the five variable candidates show significant variability (at a level $> 99\%$) in the measured fluxes.

We have made a basic comparison of the fraction of X-ray variable BAL quasars in our sample with the larger *Chandra* quasar sample of Gibson & Brandt (2012). To make an appropriate basic comparison with this sample, we obtain the average S/N of the observations of each source in our sample (see Table 8). These S/N values are converted to an equivalent number of counts in the *Chandra* full band (see Table 8). We assume that the errors in the *Chandra* counts are given by Tables 1 and 2 of Gehrels (1986). We proceed by obtaining the expected variability detection probability for each source based on the count-dependent fraction of variable sources found in §3.2 of Gibson & Brandt (2012). For this purpose, we have divided the sources in Gibson & Brandt (2012) into four count ranges: 1–10, 10–100, 100–1000, and 1000–10000 counts. The fractions (variability detection probabilities) of detectably variable sources in each range are 0.02, 0.20, 0.43, and 0.80. For each source we select one of these four values based on its equivalent average counts in the *Chandra* full band (see Table 8). Adding the probabilities found in Table 8, the expected number of variable sources is ≈ 3.5 . Therefore, the fraction of X-ray variable sources appears comparable to that expected for normal quasars. As is shown in Gibson & Brandt (2012), the fraction of detectably variable sources in X-rays has a first-order dependency on the S/N of the observations of each source. This is because the sensitivity to measure any change in the flux increases with S/N. Additionally, the UV luminosities of our sources are broadly comparable to those of the sample of Gibson & Brandt (2012), although both sets of sources span large ranges of luminosity (see Figure 5). The mean luminosity of our sample ($\langle L_{2500} \rangle = 30.95 \pm 0.31$) is similar to the mean luminosity of the sample of Gibson & Brandt (2012) ($\langle L_{2500} \rangle = 30.55 \pm 0.04$). Therefore, any secondary luminosity dependency (e.g., Nandra et al. 1997; Manners et al. 2002)¹⁶ of the variability should not fundamentally affect our basic comparisons with Gibson & Brandt (2012).

The ratio of maximum-to-minimum fluxes of the variability is 3.8 ± 1.3 , 1.5 ± 0.2 , and 9.9 ± 2.3 for PG 1001+054, PG 1004+130, and PG 2112+059, respectively. These ratios have been calculated in the 2–8 keV band since in this band all the sources present variability. Additionally, the shortest rest-frame timescales of significant variability were approximately 5.8, 1.4, and 0.5 yr for PG 1001+054, PG 1004+130, and PG 2112+059, respectively. Since in general there is not extensive coverage of sources with a single X-ray mission (with the exception of PG 2112+059 and Mrk 231), the flux uncertainties of our variability analysis are greater than 10%. Hence, for most of the sources we are not sensitive to amplitude changes $\lesssim 1.4$.¹⁷ In general the amplitude

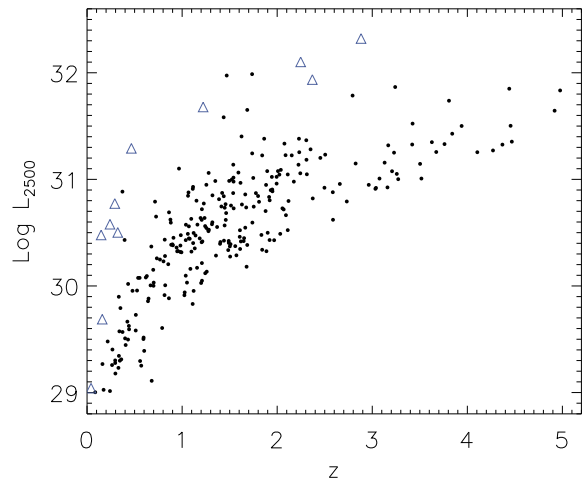


FIG. 5.— Logarithm of the monochromatic luminosity at rest-frame 2500 Å versus redshift. Monochromatic luminosities used here have units of $\text{erg s}^{-1}\text{Hz}^{-1}$. Black-filled circles are data from Gibson & Brandt (2012). Our sample is represented with open triangles.

threshold for variability detection is higher than 1.4, especially for observations with less than ~ 100 counts, for which errors in the flux are above 10%. As found in Table 8 the maximum-to-minimum flux amplitudes of the sources that do not present statistically significant variability are 10–100% in the 2–8 keV band.

Notice that in the variability searching above we have not taken into account flux upper limits. In general, as seen from Figures 2, 3, and 4, the typically loose flux upper limits do not present any new useful information regarding variability; specifically, the upper limits are usually above or not far below the best-fit constant flux. As one basic illustrative test to see if the upper limits give any new information about variability, we assume that the upper limits are detections with fluxes given by one half of the threshold and error bars that are three tenths of the upper-limit value.¹⁸ Under this assumption we test for variability by calculating the fits of constant flux in Table 7. The test with the upper limits presented in Table 7 is with 10% cross-calibration errors taken into account. From this test we find that the upper limits are possibly giving new information about variability in just one case. This case corresponds to the *Einstein* upper limit for PG 1004+130. From Figure 2 and Table 7 it is clear that the upper limit increases the significance of the soft-band variability of PG 1004+130. Since this source has already shown variability in the hard band and possibly full band, adding the upper limit does not contribute any material change to the conclusions of the variability analysis.

We also searched for rapid variability in the high signal-to-noise ratio ($S/N > 25$) *Chandra*, *XMM-Newton*, *ASCA*, and *ROSAT* observations by applying the Kolmogorov-Smirnov test to the photon arrival times. No significant variability (at a level of sig-

¹⁶ Not clear relation was found between luminosity and X-ray variability in Gibson & Brandt (2012).

¹⁷ Assuming two flux measurements with a fractional error of 10% each, our variability test requires a maximum-to-minimum flux ratio of $\gtrsim 1.4$ in order to get a $\gtrsim 99\%$ level of significance.

¹⁸ If we assume that the flux below the upper-limit has a uniform distribution, the mean value is half the threshold and σ is $\sqrt{1/12} \approx 0.28$ of the upper-limit.

¹⁶ Not clear relation was found between luminosity and X-ray variability in Gibson & Brandt (2012).

¹⁷ Assuming two flux measurements with a fractional error of

nificance $>99\%$) in the full band of each instrument was found.

As illustrated with the shaded regions in Figures 2, 3, and 4, the BAL quasars in our sample are usually X-ray weak by factors of $\approx 2\text{--}100$ relative to expectations for non-BAL quasars (see §4.3 for further discussion). Thus, any substantial removal of the shielding gas responsible for this X-ray weakness (see §1) from our line of sight should lead to large X-ray flux changes—changes that are larger than the upper limits that we typically place above upon allowed X-ray variability. The fact that such large X-ray flux changes appear rare over 3–30 yr suggests that the shielding gas is fairly stable, even on timescales sufficiently long to allow significant physical rearrangement and accretion-disk rotation. This fact should be considered in future modeling of BAL quasar X-ray absorption variability (e.g., Sim et al. 2010) as well as in interpretation of UV BAL variability results (e.g., Gibson et al. 2008, 2010; Capellupo et al. 2011, 2012; Filiz Ak et al. 2012).

4.2. Flux variability in complex spectra

For low S/N observations it is not possible to probe effectively spectral complexity that deviates from the power-law models used in §3. However, in cases where the S/N is sufficiently high we can quantify these deviations. We address this issue by grouping with a minimum of ten counts per bin the high S/N observations ($S/N > 25$) and then performing F -tests to assess the improvement of the fits from a power-law through the use of more complex alternative models.

The alternative models selected are used to probe complex absorption and to corroborate previous studies of sources in our sample (e.g., Maloney & Reynolds 2000; Gallagher et al. 2002, 2004; Schartel et al. 2005, 2010; Miller et al. 2006).¹⁹ Through this method we find that in three sources at least one of the alternative models improves the fit with significance $> 99\%$ in every high S/N observation; these sources are Mrk 231, CSO 755, and PG 2112+059. In the case of Mrk 231 there were two models (models 6 and 7 in Footnote 19) that provide improvement of the fits in every high S/N observation. These models are thermal plasma + two absorbed power-laws and thermal plasma + reflection spectrum. Note that when we use a model with two absorbed power-laws, each power-law component has the photon index fixed to $\Gamma = 2$ and the column density free to vary. The power-law that is heavily absorbed represents the intrinsic X-ray emission and the second power-law with less absorption represents scattered emission (see, e.g., Gallagher et al. 2002; Braitto et al. 2004). In the case of CSO 755 an ionized absorbed power-law model improves the fit in the only high S/N observation (in agreement with Shemmer et al. 2005). In the case of PG 2112+059 there were two models that show improvement of the fits

¹⁹ These models are (1) absorbed power-law with iron emission line, (2) ionized-absorbed power-law (XSPEC model ABSOR1), (3) partially covered absorbed power-law, (4) reflection spectrum (XSPEC model PEXRAV), (5) thermal plasma (XSPEC model VRAYMOND) + power-law, (6) thermal plasma + two absorbed power-laws (scattered spectra), (7) thermal plasma + reflection spectrum, (8) reflection spectrum from ionized media (XSPEC model PEXRIV), and (9) power-law with absorption from a blueshifted iron line.

in every high S/N observation. These models are thermal plasma + two absorbed power-laws and reflection spectrum from ionized media.

Based on these fitting results, we have recalculated the fluxes in each observation and band for Mrk 231 and PG 2112+059 using the thermal plasma + two absorbed power-law model, and for CSO 755 using an ionized-absorbed power-law model.²⁰ The fluxes obtained using these new models are presented in Table 9 and plotted in Figure 6. The models used to obtain the fluxes in Figure 6 (and Table 9) involve more parameters than a simple power-law; therefore, the error bars on the fluxes in this figure are in general somewhat larger than those obtained in Figures 2, 3, and 4. The flux-variability analysis for Mrk 231, CSO 755, and PG 2112+059 using complex models is consistent with that using a simple power-law model (see Table 7 and §4.1). Additionally, the weighted average fluxes obtained for Mrk 231, CSO 755, and PG 2112+059 through the use of more complex models are within 20% of those obtained using a power-law model (see Table 7). Therefore, as expected, our main variability results appear robust to alternative modeling of the spectra.

4.3. Spectral variability

As expected our sample of BAL quasars is generally X-ray weak when compared with RQQs of similar UV luminosities (see Table 10 and Figures 2, 3, 4, and 7). On average our sample has luminosities at rest-frame 2 keV that are ≈ 20 times weaker than expectations for RQQs (Steffen et al. 2006; Just et al. 2007). With the exceptions of CSO 755 and SBS 1542+541, which are as X-ray luminous as typical RQQs, all of our sample is $\gtrsim 3\sigma$ below the $\alpha_{\text{ox}} - L_{\text{UV}}$ and $L_{2\text{keV}} - L_{\text{UV}}$ relations (see Table 10 and Table 5 of Steffen et al. 2006). In Figure 7 we have plotted α_{ox} and $L_{2\text{keV}}$ versus L_{UV} for our sample. For the cases of X-ray variable sources we have marked the states of maximum and minimum X-ray flux in the $\alpha_{\text{ox}} - L_{\text{UV}}$ and $L_{2\text{keV}} - L_{\text{UV}}$ diagrams assuming that the UV luminosity is constant. The assumption that the UV luminosity is constant is required given that the X-ray observations do not have simultaneous optical/UV follow-up in general. However, in general it is expected that the luminosity in the UV will vary much less than that in the X-rays. For example, the *XMM-Newton* observations of PG 2112+059 present maximum-to-minimum flux ratios in the X-rays of ≈ 6 and in the optical of ≈ 1.1 (Schartel et al. 2010).

To perform a basic test for X-ray spectral variability, we utilize the effective photon index from a simple power-law fit, recognizing that this photon index may not have a direct physical interpretation in cases of complex spectra. Using the same variability test as in §4.1, we conclude that changes in Γ have significances $> 99\%$ for PG 1004+130 and PG 2112+059.²¹ For PG 2112+059

²⁰ The error in the estimated fluxes using the thermal plasma + two power-law model depends mainly on the normalization of the two power-laws (n_{PL1} and n_{PL2}), and therefore we estimate the error on the flux in a given band (f_{BP}) by $\Delta f_{\text{BP}} = \left| \frac{\partial f_{\text{BP}}}{\partial n_{\text{PL1}}} \right| \Delta n_{\text{PL1}} + \left| \frac{\partial f_{\text{BP}}}{\partial n_{\text{PL2}}} \right| \Delta n_{\text{PL2}}$.

²¹ We have taken into account the cross-calibration errors in Γ which are estimated to be $\lesssim 5\%$ (e.g., Snowden 2002; Kirsch et al. 2005; Tsujimoto et al. 2011).

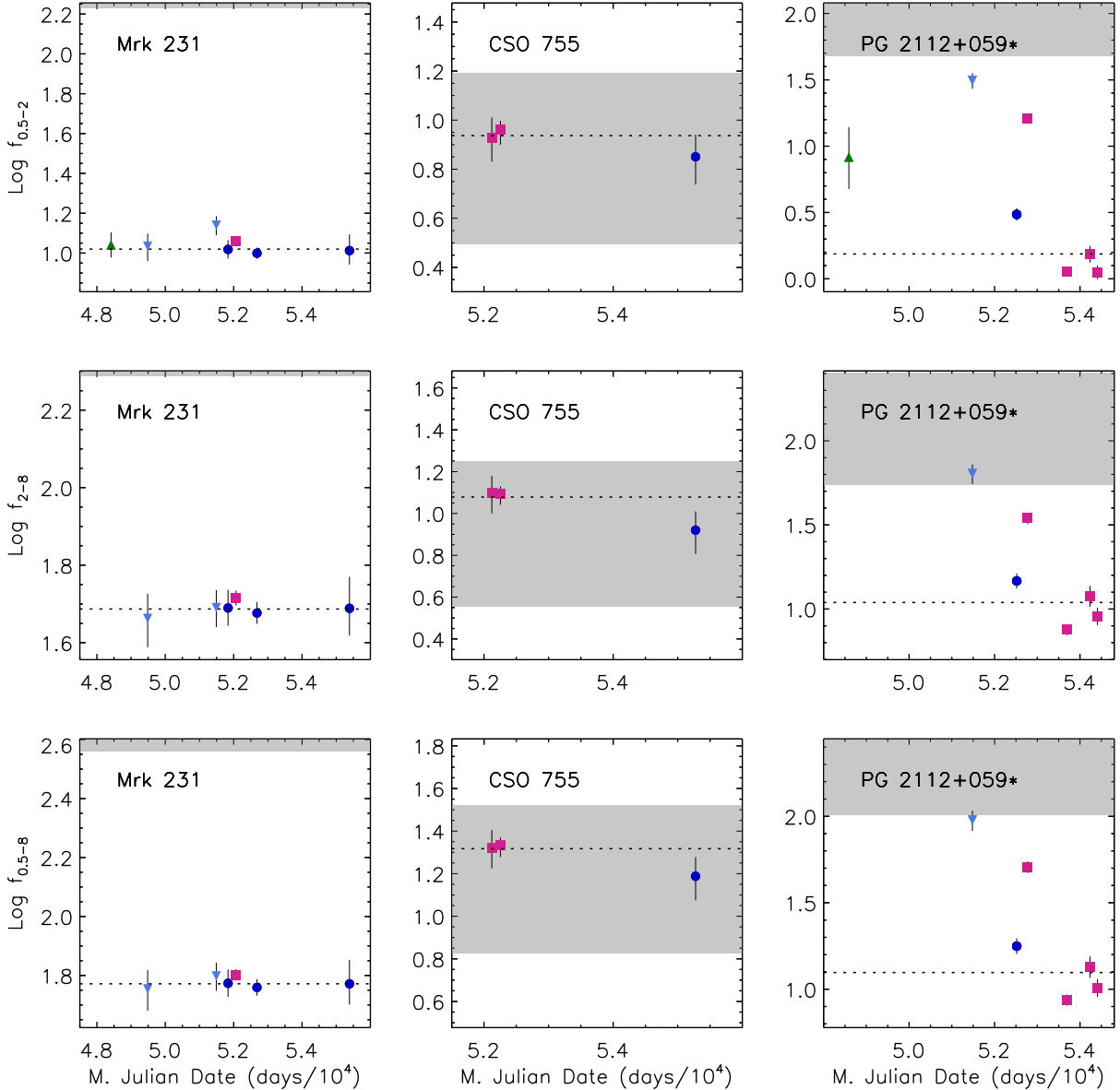


FIG. 6.— Logarithm of the observed flux (in units of 10^{-14} erg cm^{-2} s^{-1}) versus modified Julian date for Mrk 231, CSO 755, and PG 2112+059. The fluxes were obtained using alternative models to a simple power-law. The three upper, middle, and lower panels correspond to fluxes in the soft (0.5–2 keV), hard (2–8 keV) and full (0.5–8 keV) bands, respectively. The circles, squares, inverted triangles, and triangles indicate observations performed with *Chandra*, *XMM-Newton*, *ASCA*, and *ROSAT*, respectively. See the Figure 2 caption for additional details about the presentation.

the changes in Γ are confirmed with significant variability ($> 99\%$ significance) in the complex fits hard-to-soft flux ratios ($f_{2-8}/f_{0.5-2}$) (see, e.g., Table 9). In the case of PG 1001+054, the low S/N of the *Chandra* observation does not allow us to constrain the photon index well, and therefore we cannot tell if there is any change in the shape of the spectra. We conclude that the flux variability of PG 1004+130 and PG 2112+059 shows associated spectral variability.

From our spectral analyses alone it is not possible to explain the extreme weakness of the X-ray luminosities of our sources; however, this is likely associated with complex absorption. As already noted in §3 almost half of our sample (five out of eleven) presents direct evidence of absorption. Additionally, the flat effective spectral indices measured for most of the sample could be an indication of absorption. For example, as

described in Miller et al. (2006), the hard spectrum of PG 1004+130 could imply partially covering absorption. Furthermore, based on our spectral analyses it is likely that the observations of Mrk 231 and the weak states of PG 2112+059 correspond to epochs of heavy absorption ($N_{\text{H}} > 10^{23}$ cm^{-2}). Therefore, the complexity in the observed spectra of these sources could be the result of heavily absorbed emission plus scattered emission (see §4.2). In the case of Mrk 231 this picture has been shown to be plausible in the joint spectral analysis of *XMM-Newton* and *BeppoSAX* observations at energies between 0.2–50 keV performed by Braito et al. (2004). The spectral softening of PG 2112+059 with increasing flux might be explained by an increase in the observable X-ray emission due to a decrease in the absorption (see §4.2). Alternative interpretations of the physical picture for PG 2112+059 (e.g., a reflection dominated spectrum)

TABLE 10
OPTICAL AND X-RAY PROPERTIES OF SURVEYED BAL QUASARS

OBJECT NAME	Log L_{2500}^a	Log L_{2-10}^b	Log $L_{2\text{keV}}^c$	$\Delta\text{Log } L_{2\text{keV}}^d$	Log f_{2-8}^e	$\Delta\text{Log } f_{2-8}^f$	α_{ox}^g	$\Delta\alpha_{\text{ox}}^h$
IRAS 07598+6508	30.48	41.87	24.18	-2.26	-14.01	-2.53	-2.42±0.06	-0.85
PG 0946+301	31.68	44.74	25.42	-1.86	-12.99	-0.23	-2.40±0.08	-0.66
PG 1001+054	29.69	42.34	24.22	-1.65	-13.81	-1.70	-2.10±0.07	-0.64
PG 1004+130	30.58	43.82	25.61	-0.89	-12.50	-0.62	-1.91±0.05	-0.32
Q 1246-057	32.10	44.94	26.65	-0.93	-13.55	-0.46	-2.09±0.05	-0.29
Mrk 231	29.04	42.36	24.08	-1.33	-12.36	-1.02	-1.90±0.04	-0.53
IRAS 14026+4341	30.50	42.78	24.80	-1.65	-13.83	-1.61	-2.19±0.10	-0.62
CSO 755	32.32	45.88	27.63	-0.11	-12.94	0.25	-1.80±0.05	0.02
SBS 1542+541	31.94	45.51	27.32	-0.15	-13.06	0.21	-1.77±0.05	-0.00
PG 1700+518	30.77	42.48	24.48	-2.16	-14.03	-2.11	-2.42±0.06	-0.80
PG 2112+059	31.29	43.99	25.40	-1.61	-13.02	-0.99	-2.26±0.04	-0.57

^a Logarithm of the monochromatic luminosity at rest-frame 2500 Å (with units $\text{erg s}^{-1} \text{Hz}^{-1}$). These values were computed from the flux densities at rest-frame wavelength 2500 Å using the corrected for galactic reddening flux densities of the closest optical magnitude and extrapolating a power-law with $\alpha = -0.5$ (e.g., Vanden Berk et al. 2001).

^b Logarithm of the 2–10 keV band luminosity (with units erg s^{-1}). For each source this quantity was obtained from the weighted-average luminosities of the *Chandra*, *XMM-Newton*, and *ASCA* observations in the 2–10 keV rest-frame band. The luminosities have been corrected for Galactic absorption.

^c Logarithm of the monochromatic luminosity at rest-frame 2 keV (with units $\text{erg s}^{-1} \text{Hz}^{-1}$). For each source this quantity was obtained from the weighted-average flux of the *Chandra*, *XMM-Newton*, *ASCA*, and *ROSAT* observations at 2 keV rest-frame.

^d The difference between the measured and the predicted $\log L_{2\text{keV}}$ for RQQs, based on the Just et al. (2007) relation: $\log L_{2\text{keV}} = 0.709 \times \log L_{2500} + 4.822$.

^e Logarithm of the flux in the 2–8 keV band (in units of $10^{-14} \text{erg cm}^{-2} \text{s}^{-1}$). For each source this flux was obtained from the weighted-average flux of the *Chandra*, *XMM-Newton*, *BeppoSAX*, and *ASCA* observations in the 2–8 keV band.

^f The difference between the measured and the predicted flux in the 2–8 keV band for RQQs. The predicted fluxes in the 2–8 keV band are obtained from the expected fluxes for RQQs at 2 keV rest-frame (Just et al. 2007) assuming a power-law spectrum with $\Gamma = 1.9$.

^g The optical-to-X-ray power-law slope $\alpha_{\text{ox}} = \log(f_{2\text{keV}}/f_{2500\text{\AA}})/\log(\nu_{2\text{keV}}/\nu_{2500\text{\AA}})$.

^h The difference between the measured α_{ox} value and the predicted α_{ox} for RQQ, based on the Just et al. (2007) relation: $\alpha_{\text{ox}} = -0.140 \times \log L_{2500\text{\AA}} + 2.705$.

can be found in Schartel et al. (2010). The *ASCA* observation of PG 2112+059 presents a typical quasar spectral shape with absorption that is moderate enough so the majority of the X-ray emission can get through the absorber. Therefore, the X-ray emission of PG 2112+059 in its brightest state is likely to be dominated by unabsorbed emission over scattered emission. The hardening of the spectra with increasing flux for PG 1004+130 is not easily explained with absorption alone; its origin could be more complex due to X-ray jet-linked emission (for details see Miller et al. 2006). Future X-ray observations, especially with high sensitivity above 10 keV such as those with *NuSTAR* and *ASTRO-H*, will help to clarify the physical picture of these sources.

5. SUMMARY AND FUTURE WORK

We have analyzed *Chandra*, *XMM-Newton*, *BeppoSAX*, *ASCA*, *ROSAT*, and *Einstein* observations of eleven BAL quasars to perform the first systematic investigation of the long-term X-ray variability of this population on rest-frame timescales of 3–30 yr. For seven out of the eleven sources we have also obtained and reported on new *Chandra* observations suitable for detecting any strong X-ray variability. Our main conclusions are the following:

1. We find that three (PG 1001+054, PG 1004+130, and PG 2112+059) of the eleven sources show significant flux variability (at a confidence level > 99%). The maximum observed amplitude of this variability in the 2–8 keV band is a factor of 3.8 ± 1.3 , 1.5 ± 0.2 , and 9.9 ± 2.3 for PG 1001+054, PG 1004+130, and PG 2112+059, respectively. These three sources show detectable variability on rest-frame timescales down to 5.8, 1.4, and 0.5 yr,

respectively. See §4.1 and §4.2.

2. The flux variability of PG 1004+130 and PG 2112+059 has associated spectral variability (the data for PG 1001+054 do not allow effective investigation of spectral variability). This spectral variability may be induced by absorption changes, although the hardening of PG 1004+130 when it brightens is puzzling in this regard. See §4.3.
3. The eight sources in our sample without significantly detected X-ray flux variability are constrained by our data to have varied by less than 10–100%. See §4.1.
4. We do not find that BAL quasars exhibit exceptional long-term X-ray variability when comparing the measured variability for our whole sample to that of non-BAL quasars. Strong changes in the X-ray absorbing shielding gas, owing to physical rearrangement or accretion-disk rotation, appear relatively rare (although some changes are present). Since the shielding gas is critical for setting the ionization level of the wind that produces UV BALs, our results have implications for modeling BAL variability. See §4.1.
5. We report for the first time an X-ray detection of the highly polarized and well-studied BAL quasar IRAS 14026+4341. We detect this source with a statistical significance of $\approx 5\sigma$ in our new *Chandra* observation. See §2.6.

This first systematic investigation has significantly improved constraints upon the long-term X-ray variability

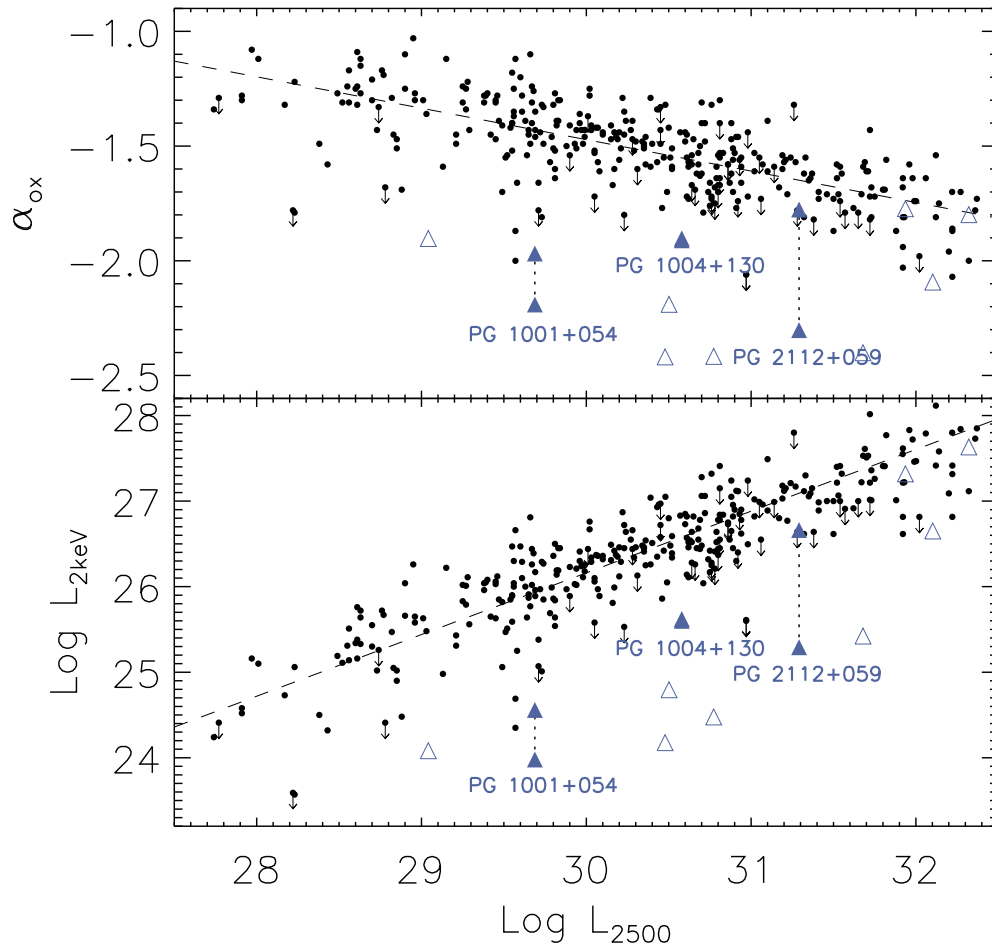


FIG. 7.— Logarithm of the monochromatic luminosity at rest-frame 2500 Å versus α_{ox} (upper panel) and logarithm of the monochromatic luminosity at rest-frame 2 keV (lower panel). Monochromatic luminosities used here have units of $\text{erg s}^{-1} \text{Hz}^{-1}$. Black-filled circles are data from Steffen et al. (2006); arrows indicate X-ray upper limits. Dashed lines are the best-fit linear relations for their combined sample. Our sample is represented with filled and open triangles for sources with and without variability, respectively. For variable sources we have plotted the state of minimum and maximum flux joined with a dotted line. PG 1004+130 does not show variability in soft X-rays, and therefore its 2 keV luminosity is presented as a single point.

of BAL quasars in general. However, further improvements are needed in the number of objects monitored, the number of monitoring epochs, the number of detected counts per epoch, and the bandpass coverage. Improving the numbers of objects and epochs will set better constraints upon the frequency of significant absorption changes; this could be achieved with, e.g., additional *Chandra* and *XMM-Newton* observations. Improving the number of detected counts per epoch or extending the bandpass coverage to higher energies will enable better physical understanding when absorption changes are detected; missions including *NuSTAR*, *ASTRO-H*, and *Athena* are required for such observations.

We thank the referee for constructive feedback. We gratefully acknowledge support from NASA ADP grant NNX10AC99G (CS, WNB), NSF grant AST-1108604 (WNB), and NASA grant SAO SV4-74018 (GPG, Principal Investigator). SCG thanks the Natural Science and Engineering Research Council of Canada and the On-

tario Early Researcher Award Program for their support. FEB and CS acknowledge support from Programa de Financiamiento Basal and CONICYT-Chile under grants FONDECYT 1101024 and 3120198 and fondap-cata 15010003. This research has made use of the Tartarus (Version 3.1) database, created by Paul O’Neill and Kirpal Nandra at Imperial College London, and Jane Turner at NASA/GSFC. Tartarus was supported by funding from PPARC, and NASA grants NAG5-7385 and NAG5-7067.

REFERENCES

- Avni, Y. 1976, *ApJ*, 210, 642
- Ballo, L., Piconcelli, E., Vignali, C., & Schartel, N. 2011, *MNRAS*, 415, 2600
- Barlow, R. 2004, *ArXiv Physics e-prints/0406120v1*
- Boksenberg, A., Carswell, R. F., Allen, D. A., Fosbury, R. A. E., Penston, M. V., & Sargent, W. L. W. 1977, *MNRAS*, 178, 451
- Boroson, T. A., & Meyers, K. A. 1992, *ApJ*, 397, 442
- Braito, V., et al. 2004, *A&A*, 420, 79
- Brandt, W. N., Comastri, A., Gallagher, S. C., Sambruna, R. M., Boller, T., & Laor, A. 1999, *ApJ*, 525, L69
- Broos, P. S., Townsley, L. K., Feigelson, E. D., Getman, K. V., Bauer, F. E., & Garmire, G. P. 2010, *ApJ*, 714, 1582
- Capellupo, D. M., Hamann, F., Shields, J. C., Rodríguez Hidalgo, P., & Barlow, T. A. 2011, *MNRAS*, 413, 908
- . 2012, *MNRAS*, 422, 3249
- Cash, W. 1979, *ApJ*, 228, 939
- Chartas, G., Saez, C., Brandt, W. N., Giustini, M., & Garmire, G. P. 2009, *ApJ*, 706, 644
- Condon, J. J., Cotton, W. D., Greisen, E. W., Yin, Q. F., Perley, R. A., Taylor, G. B., & Broderick, J. J. 1998, *AJ*, 115, 1693
- Di Matteo, T., Springel, V., & Hernquist, L. 2005, *Nature*, 433, 604
- Dickey, J. M., & Lockman, F. J. 1990, *ARA&A*, 28, 215
- Elvis, M., & Fabbiano, G. 1984, *ApJ*, 280, 91
- Everett, J. E. 2005, *ApJ*, 631, 689
- Fan, L. L., Wang, H. Y., Wang, T., Wang, J., Dong, X., Zhang, K., & Cheng, F. 2009, *ApJ*, 690, 1006
- Filiz Ak, N., et al. 2012, *ApJ*, in press
- Gallagher, S. C., Brandt, W. N., Sambruna, R. M., Mathur, S., & Yamasaki, N. 1999, *ApJ*, 519, 549
- Gallagher, S. C., Brandt, W. N., Laor, A., Elvis, M., Mathur, S., Wills, B. J., & Iyomoto, N. 2001, *ApJ*, 546, 795
- Gallagher, S. C., Brandt, W. N., Chartas, G., & Garmire, G. P. 2002, *ApJ*, 567, 37
- Gallagher, S. C., Brandt, W. N., Chartas, G., Garmire, G. P., & Sambruna, R. M. 2002, *ApJ*, 569, 655
- Gallagher, S. C., Brandt, W. N., Wills, B. J., Charlton, J. C., Chartas, G., & Laor, A. 2004, *ApJ*, 603, 425
- Gallagher, S. C., Schmidt, G. D., Smith, P. S., Brandt, W. N., Chartas, G., Hylton, S., Hines, D. C., & Brotherton, M. S. 2005, *ApJ*, 633, 71
- Gallagher, S. C., Brandt, W. N., Chartas, G., Priddey, R., Garmire, G. P., & Sambruna, R. M. 2006, *ApJ*, 644, 709
- Ganguly, R., & Brotherton, M. S. 2008, *ApJ*, 672, 102
- Gehrels, N. 1986, *ApJ*, 303, 336
- Gibson, R. R., Brandt, W. N., Schneider, D. P., & Gallagher, S. C. 2008, *ApJ*, 675, 985
- Gibson, R. R., et al. 2009, *ApJ*, 692, 758
- Gibson, R. R., Brandt, W. N., Gallagher, S. C., Hewett, P. C., & Schneider, D. P. 2010, *ApJ*, 713, 220
- Gibson, R. R., & Brandt, W. N. 2012, *ApJ*, 746, 54
- Green, P. J., & Mathur, S. 1996, *ApJ*, 462, 637
- Green, P. J., Aldcroft, T. L., Mathur, S., Wilkes, B. J., & Elvis, M. 2001, *ApJ*, 558, 109
- Grupe, D., Mathur, S., & Elvis, M. 2003, *AJ*, 126, 1159
- Gültekin, K., et al. 2009, *ApJ*, 698, 198
- Hines, D. C., Schmidt, G. D., Gordon, K. D., Smith, P. S., Wills, B. J., Allen, R. G., & Sitko, M. L. 2001, *ApJ*, 563, 512
- Imanishi, M., & Terashima, Y. 2004, *AJ*, 127, 758
- Just, D. W., Brandt, W. N., Shemmer, O., Steffen, A. T., Schneider, D. P., Chartas, G., & Garmire, G. P. 2007, *ApJ*, 665, 1004
- Kellermann, K. I., Sramek, R., Schmidt, M., Shaffer, D. B., & Green, R. 1989, *AJ*, 98, 1195
- Kirsch, M. G., et al. 2005, in *Society of Photo-Optical Instrumentation Engineers (SPIE) Conference Series*, Vol. 5898, *Society of Photo-Optical Instrumentation Engineers (SPIE) Conference Series*, ed. O. H. W. Siegmund, 22–33
- Laor, A., Fiore, F., Elvis, M., Wilkes, B. J., & McDowell, J. C. 1997, *ApJ*, 477, 93
- Laor, A., & Brandt, W. N. 2002, *ApJ*, 569, 641
- Lawrence, A., Elvis, M., Wilkes, B. J., McHardy, I., & Brandt, N. 1997, *MNRAS*, 285, 879
- Maloney, P. R., & Reynolds, C. S. 2000, *ApJ*, 545, L23
- Manners, J., Almaini, O., & Lawrence, A. 2002, *MNRAS*, 330, 390
- Mathur, S., et al. 2000, *ApJ*, 533, L79
- Miller, B. P., Brandt, W. N., Gallagher, S. C., Laor, A., Wills, B. J., Garmire, G. P., & Schneider, D. P. 2006, *ApJ*, 652, 163
- Mukai, K. 1993, *Legacy*, vol. 3, p.21–31, 3, 21
- Murray, N., Chiang, J., Grossman, S. A., & Voit, G. M. 1995, *ApJ*, 451, 498
- Murray, N., & Chiang, J. 1997, *ApJ*, 474, 91
- Nandra, K., George, I. M., Mushotzky, R. F., Turner, T. J., & Yaqoob, T. 1997, *ApJ*, 476, 70
- Nevalainen, J., David, L., & Guainazzi, M. 2010, *A&A*, 523, A22
- Page, M. J., Carrera, F. J., Stevens, J. A., Ebrero, J., & Blustin, A. J. 2011, *MNRAS*, 416, 2792
- Petric, A. O., Carilli, C. L., Bertoldi, F., Beelen, A., Cox, P., & Omont, A. 2006, *AJ*, 132, 1307
- Proga, D., Stone, J. M., & Kallman, T. R. 2000, *ApJ*, 543, 686
- Richards, G. T., et al. 2011, *AJ*, 141, 167
- Rigopoulou, D., Lawrence, A., & Rowan-Robinson, M. 1996, *MNRAS*, 278, 1049
- Risaliti, G., Elvis, M., & Nicastro, F. 2002, *ApJ*, 571, 234
- Risaliti, G., et al. 2009, *MNRAS*, 393, L1
- Ruiz, A., Carrera, F. J., & Panessa, F. 2007, *A&A*, 471, 775
- Saez, C., & Chartas, G. 2011, *ApJ*, 737, 91
- Schartel, N., Rodríguez-Pascual, P. M., Santos-Lleó, M., Clavel, J., Guainazzi, M., Jiménez-Bailón, E., & Piconcelli, E. 2005, *A&A*, 433, 455
- Schartel, N., Rodríguez-Pascual, P. M., Santos-Lleó, M., Ballo, L., Clavel, J., Guainazzi, M., Jiménez-Bailón, E., & Piconcelli, E. 2007, *A&A*, 474, 431
- Schartel, N., Rodríguez-Pascual, P. M., Santos-Lleó, M., Jiménez-Bailón, E., Ballo, L., & Piconcelli, E. 2010, *A&A*, 512, A75
- Shemmer, O., Brandt, W. N., Gallagher, S. C., Vignali, C., Boller, T., Chartas, G., & Comastri, A. 2005, *AJ*, 130, 2522
- Sim, S. A., Proga, D., Miller, L., Long, K. S., & Turner, T. J. 2010, *MNRAS*, 408, 1396
- Snowden, S. L. 2002, *ArXiv:astro-ph/0203311*
- Steffen, A. T., Strateva, I., Brandt, W. N., Alexander, D. M., Koekemoer, A. M., Lehmer, B. D., Schneider, D. P., & Vignali, C. 2006, *AJ*, 131, 2826
- Tsujiimoto, M., et al. 2011, *A&A*, 525, A25
- Vanden Berk, D. E., et al. 2001, *AJ*, 122, 549
- Wang, T., Brinkmann, W., & Bergeron, J. 1996, *A&A*, 309, 81
- Weisskopf, M. C., Guainazzi, M., Jahoda, K., Shaposhnikov, N., O'Dell, S. L., Zavlin, V. E., Wilson-Hodge, C., & Elsner, R. F. 2010, *ApJ*, 713, 912
- White, R. L., Becker, R. H., Helfand, D. J., & Gregg, M. D. 1997, *ApJ*, 475, 479
- Wilkes, B. J., Tananbaum, H., Worrall, D. M., Avni, Y., Oey, M. S., & Flanagan, J. 1994, *ApJS*, 92, 53
- Wu, J., Brandt, W. N., Comins, M. L., Gibson, R. R., Shemmer, O., Garmire, G. P., & Schneider, D. P. 2010, *ApJ*, 724, 762